Computational Analysis and Regression Laws for Nozzle Erosion Prediction in Hybrid Rockets

Marco Rotondi*, Mario Tindaro Migliorino†, and Daniele Bianchi‡
Sapienza University of Rome, 00184 Rome, Italy

Landon Kamps§ and Harunori Nagata¶
Hokkaido University, Sapporo, 060-8628, Japan

The erosion of the nozzle throat can represent one of the major limitations against the future widespread use of hybrid rocket engines (HRE) in the space industry. In fact, nozzle erosion in HRE can be more severe and harder to predict than in solid rockets due to the higher concentration of oxidizing species in the combustion products and to mixture ratio shifts and/or throttling. Therefore, an accurate understanding of the erosion phenomenon is of fundamental importance for the technological advancement of HRE. This work is focused on the investigation of graphite nozzle erosion in HRE burning high-density polyethylene (HDPE) with two different oxidizers, oxygen and nitrous oxide. Firstly, results of a computational fluid dynamics (CFD) parametric analysis are used to derive closed-form regression laws for the rapid estimation of nozzle throat erosion and wall temperature depending on chamber pressure and mixture ratio. Then, a one-dimensional transient heat conduction solver is loosely coupled with the aforementioned regression laws, allowing to reconstruct the transient heating process within the solid. The obtained numerical results are validated against experimental data. Finally, the effect of gas-phase reactions on the heterogeneous reactions occurring at the nozzle surface is highlighted when moving from fuel-rich to oxidizer-rich conditions.

Nomenclature

c = specific heat, $\mathrm{J/(kg \cdot K)}$

D = diameter, m

Presented as AIAA paper 2021-3496 at the 2021 AIAA Propulsion & Energy (PE) Forum, Virtual Event, 09-11 August 2021

*Ph.D. Student, Department of Mechanical and Aerospace Engineering, Via Eudossiana 18, Member AIAA, corresponding author, marco.rotondi@uniroma1.it

†Research Assistant Professor, Department of Mechanical and Aerospace Engineering, Via Eudossiana 18, Member AIAA

‡Associate Professor, Department of Mechanical and Aerospace Engineering, Via Eudossiana 18, Member AIAA

§Specially appointed Assistant Professor, Faculty of Engineering, Department of Mechanical and Space Engineering, Member AIAA

¶Professor, Faculty of Engineering, Department of Mechanical and Space Engineering, Member AIAA

f	=	generic numerical solution
h	=	enthalpy, $\mathrm{J/kg}$
k	=	thermal conductivity, $\mathrm{W/(m \cdot K)}$
$\dot{m}$	=	ablation mass flux, $\mathrm{kg/(m^2 \cdot s)}$
n	=	spatial order of accuracy
p	=	pressure, $\mathrm{N/m^2}$
R^2	=	goodness of fit
R	=	radius, m
$\mathfrak{R}$	=	universal gas constant, $\mathrm{J/(mol \cdot K)}$
$\dot{\mathrm{r}}$	=	erosion rate, $\mathrm{m/s}$
T	=	temperature, K
t	=	time, s
$\mathbf{v}$	=	flow velocity, m/s
W	=	molar mass, kg/mol
y	=	mass fraction
y^+	=	dimensionless wall distance
ε	=	relative numerical error
η	=	wall-normal coordinate
η_{c^*}	=	combustion efficiency
ρ	=	density, $\mathrm{kg/m^3}$
σ	=	Stefan–Boltzmann constant, $\mathrm{W/(m^2 \cdot K^4)}$
$\dot{\omega}$	=	species source term, $\mathrm{kg/m^2 s}$

Subscripts

b	=	of burning
c	=	combustion chamber
coarse	=	coarse mesh
fine	=	fine mesh
i	=	of the i-th species
j	=	of the j-th species or reaction
medium	=	medium mesh
RE	=	Richardson-extrapolated
s	=	solid material

st = stoichiometric

onset = beginning of erosion

th = at nozzle throat

w = wall

0 = at the initial time

I. Introduction

Hybrid rocket engines (HRE) aim to achieve system flexibility, simplicity, inherent safety (due to the separation between fuel and oxidizer), reduced development costs, and reduced environmental pollution. Despite the low regression rate of conventional pyrolyzing fuels, low bulk density, sometimes low combustion efficiency, and O/F shift [1], the above mentioned features give to hybrid rockets the potential to become a valid alternative in selected future-generation propulsion systems [2]. Nevertheless, hybrid rocket development is hindered by a partial understanding of the major underlying physical phenomena, and has not achieved the same level of maturity as traditional solid and liquid systems [3]. One of the most important aspects that constitute a challenge in hybrid rocket propulsion is the minimization of nozzle erosion, which can lead to specific impulse loss and modification of the thrust curve.

It has been shown that throat erosion rate in HRE is generally greater than that of a corresponding solid propellant system and is a strong function of chamber pressure and mixture ratio [3–7]. Indeed, the ablation process in hybrid rockets is exacerbated due to the high concentration of oxidizing species in the exhaust products, which largely affect the material thermochemical behaviour [4, 8]. The high and often hardly predictable nozzle erosion rate in HRE is one of the main responsible for their low technology readiness level [9], and for their limited application in the space industry. Therefore, the need to correctly predict and reduce nozzle throat erosion has generated a renewed interest in experimental testing [10–13] and numerical investigations [7, 14–17].

The state-of-the-art numerical evaluation of nozzle erosion should properly model the physical and chemical interaction between the protective material and the combustion gases [5], without relying on semi-empirical correlations [4]. Moreover, possible transient effects, which may be relevant especially for short duration firings, need to be properly taken into account. In fact, during transients, the surface temperature rises from an initial value towards its steady-state value and so does the erosion rate. This is responsible for the experimentally observed delay in the onset of erosion in HRE [10, 18], hence its numerical evaluation and prediction can be of great importance. In addition, a transient analysis is required in order to estimate the thermal penetration thickness during the engine firing, which is a fundamental parameter needed for the sizing of the ablative thermal protection system that can not be obtained from steady-state ablation numerical approaches [7, 14]. In this context, this work aims to investigate the steady-state and transient in-depth response of graphite nozzles at different operating conditions in HRE burning HDPE with two different

oxidizers, oxygen and nitrous oxide.

The manuscript is organized as follows. Section II is dedicated to an overview of the gas-surface interaction model used and to a brief description of the one-dimensional transient heat conduction model employed. In section III.A, an overview of the 100N-thrust class hybrid rocket static firing tests, used as reference test campaign in this work, is presented. The detailed computational set-up for the nozzles employed is shown in Sec. III.B, jointly with a grid convergence analysis. In Sec. IV, parametric numerical simulations are performed, with the aim of analyzing nozzle erosion and heating behavior at varying chamber pressure, mixture ratio, and nozzle geometry. Closed-form regression laws for nozzle throat erosion rate and wall temperature (derived by the previously mentioned parametric numerical analysis) are then provided in in Sec. IV.E. These regression laws are able to correctly handle chamber pressure, mixture ratio, and nozzle geometrical effects on the ablation process with zero computational effort and can be effectively used in multidisciplinary design optimization analyses of HREs [19]. A validation of the regression law is performed against the available experimental data in Sec. IV.F. Then, in Sec. V, a one-dimensional transient heat conduction solver is loosely coupled with the aforementioned regression laws, allowing to solve the heating process within the solid with very limited computational efforts. The results obtained are validated against the available thermocouples data. Finally, an analysis on possible gas-phase reaction effects on the nozzle ablation process is shown in Sec. VI. The increasing importance of gas-phase reactions when moving from fuel-rich to oxidizer-rich mixture ratios is highlighted comparing the results obtained with experimental data.

II. Theoretical and numerical model

The CFD approach employed in this work solves the turbulent Reynolds-averaged Navier–Stokes equations for compressible single-phase flows including variable thermodynamic and transport properties. The CFD solver is coupled to a model for carbon–carbon and graphite nozzle erosion developed and validated in previous studies of solid and hybrid rockets [5–7, 20–28]. A detailed description of the CFD code and of its sub-models is reported in the following sections.

In the CFD code, heat conduction in the nozzle is assumed to be one-dimensional and at steady-state. However, in the present work, transient heat conduction effects are taken into account employing a dedicated one-dimensional transient heating solver. In particular, a first effort towards an effective transient heating analysis consists in a time-variable Dirichlet boundary condition imposing a prescribed wall temperature and recession obtained from CFD-derived closed-form regression laws, as it will be described in details in the following sections.

A. Numerical code

In the CFD solver, the governing equations for the gas phase are the turbulent Reynolds-averaged Navier-Stokes equations for a generic reacting mixture of perfect gases with varying thermophysical properties [29]:

$$\begin{cases} \dfrac{\partial(\rho y_i)}{\partial t} + \nabla \cdot (\rho \mathbf{v} y_i) = -\nabla \cdot \mathbf{j}_i + \dot{\omega}_i \qquad i = 1, ..., N \\ \dfrac{\partial(\rho \mathbf{v})}{\partial t} + \nabla \cdot (\rho \mathbf{v}\mathbf{v}) = \nabla \cdot \mathbf{S} \\ \dfrac{\partial(\rho e_0)}{\partial t} + \nabla \cdot (\rho e_0 \mathbf{v}) = \nabla \cdot (\mathbf{v} \cdot \mathbf{S}) - \nabla \cdot \mathbf{q} \end{cases} \tag{1}$$

The term $\mathbf{j}_i$ is the diffusion mass flux of the ith species, the term $\mathbf{S}$ is the stress tensor; split into the contribution of pressure forces and viscous stresses; and the term $\mathbf{q}$ is the heat flux vector:

$$\mathbf{j}_i = -\rho(D_{im} + D_{mt})\nabla y_i \tag{2}$$

$$\mathbf{S} = -\mathrm{p}\mathbf{I} + \mathbf{T} \tag{3}$$

$$\mathbf{T} = -\frac{2}{3}(\mu + \mu_t)(\nabla \cdot \mathbf{v})\mathbf{I} + (\mu + \mu_t)\left[\nabla \mathbf{v} + (\nabla \mathbf{v})^T\right] \tag{4}$$

$$\mathbf{q} = -(k + k_t)\nabla T + \sum_{i=1}^{N} \left(h_i + \Delta h_{\mathrm{f},i}^{T_{\mathrm{ref}}}\right)\mathbf{j}_i \tag{5}$$

where $\mathbf{I}$ is the unit tensor. The term $e_0 = e + |\mathbf{v}|^2/2$ represents the total energy per unit mass of the flow which is the sum of the internal energy of the mixture $e = \sum_{i=1}^{N} y_i(e_i + \Delta e_{\mathrm{f},i}^{T_{\mathrm{ref}}})$ and the kinetic energy. The internal energy and the enthalpy of individual species, e_i and h_i, are assumed to vary only with temperature through the heat capacity at constant volume and the heat capacity at constant pressure, respectively, which are approximated by seventh-order polynomials of temperature within given temperature ranges [30]. From the same chemical database [30], the standard formation enthalpy at the reference temperature $\Delta h_{\mathrm{f},i}^{T_{\mathrm{ref}}}$ are taken. The diffusional mass flux of the ith species is expressed by Eq. (2) using the approximation of Fick's law. The terms μ, k, and D_{im} are the molecular viscosity, thermal conductivity and molecular diffusivity of the multicomponent mixture, respectively, while the terms μ_t, k_t, and D_{mt} are the corresponding eddy (or turbulent) viscosity, thermal conductivity and diffusivity, respectively. The molecular transport properties are approximated by fourth order polynomials of temperature [30]. The mixture properties for molecular viscosity μ and molecular thermal conductivity k are derived from Wilke's rule. Due to the important role in the correct prediction of the ablation mass flux played by the oxidizing species diffusion in the boundary layer, a multicomponent molecular diffusion model based on the effective diffusion coefficients is employed [25, 31].

The Spalart-Allmaras [32] one-equation model is used to compute the turbulent viscosity μ_t. The turbulent thermal conductivity k_t and the turbulent mass diffusivity D_{mt} are computed from turbulent Prandtl Pr_t (assumed equal to 0.9) and turbulent Schmidt Sc_t (assumed equal to 0.75 for near-wall flows) numbers, respectively. The Navier-Stokes

equations are numerically solved by a second-order finite difference approach that follows the lambda scheme [33] using a curvilinear orthogonal frame in order to have a grid well adapted to the geometry of the body, which is transformed to a Cartesian grid by conformal mapping.

B. Nozzle thermochemical erosion

The CFD solver described in the previous section is coupled to a gas-surface-interaction model for carbon-carbon and graphite nozzle erosion. In particular, the thermochemical ablation of the graphitic nozzle is modeled via surface mass and energy balances and takes into account heterogeneous chemical reactions at the nozzle surface, rate of diffusion of the species through the boundary layer, and ablation species injection in the boundary layer. The general conservation laws at the gas–solid interface employed in this work for a non-decomposing material such as graphite are those originally proposed in [34] and adopted and validated in previous works [5–7, 20, 21, 23–25, 28].

Table 1 Heterogeneous rate constants of carbon with H_2O, CO_2, OH, O, and O_2 [35, 36]

Surface reaction	j	A_j	E_j, kJ/mol	b_j	n_j
$C_s + H_2O \Rightarrow CO + H_2$	1	$4.8 \cdot 10^5$	288	0.0	0.5
$C_s + CO_2 \Rightarrow 2\,CO$	2	$9.0 \cdot 10^3$	285	0.0	0.5
$C_s + OH \Rightarrow CO + H$	3	$3.61 \cdot 10^2$	0.0	-0.5	1.0
$C_s + O \Rightarrow CO$	4	$6.655 \cdot 10^2$	0.0	-0.5	1.0
$C_s + \frac{1}{2}O_2 \Rightarrow CO$	5	$2.4 \cdot 10^3$	125.6	0.0	-
	6	$2.13 \cdot 10^1$	-17.17	0.0	-
	7	$5.35 \cdot 10^{-1}$	63.64	0.0	-
	8	$1.81 \cdot 10^7$	406.1	0.0	-

The heterogeneous chemical reactions taking place at the nozzle surface are modeled by the semi-global graphite oxidation kinetics proposed originally by Bradley et al. [35] and then adopted by Chelliah et al. for non-porous graphite [36] (Table 1). With this mechanism, the contribution to erosion due to the i-th species can be expressed in kg/(m$^2 \cdot$ s) as:

$$\dot{m}_{\mathrm{w},i} = \mathrm{k}_j \mathrm{p}_i^{n_j} \qquad \text{for species } i = \mathrm{H_2O}, \mathrm{CO_2}, \mathrm{OH}, \text{ and } \mathrm{O} \tag{6}$$

where p_i is the partial pressure (in atm) of the oxidizing species i, and n_j is the overall order of the heterogeneous j-th reaction. The partial pressures of each species can be derived from the thermal equation of state $\mathrm{p}_i = \rho y_i \Re T / W_i$ where $\mathrm{p} = \sum_{i=1}^{N} \mathrm{p}_i$. The term k_j is its specific rate constant, which can be expressed by an Arrhenius type expression of the form:

$$\mathrm{k}_j = A_j T_\mathrm{w}^{b_j} \exp(-E_j / \Re T_\mathrm{w}) \tag{7}$$

where T_w is the wall temperature (in Kelvin) and A_j, b_j, and E_j are the pre-exponential factor, the temperature exponent,

and the activation energy for the j-th reaction, respectively. The contribution to erosion of molecular oxygen can not be properly expressed by a single Arrhenius equation and, therefore, the expression by Nagle and Strickland-Constable [37] is used:

$$\dot{m}_{\mathrm{w},i} = \frac{\mathrm{k}_5 \mathrm{p}_i Y}{1 + \mathrm{k}_6 \mathrm{p}_i} + \mathrm{k}_7 \mathrm{p}_i (1 - Y) \qquad \text{where } Y = \left(1 + \frac{\mathrm{k}_8}{\mathrm{k}_7 \mathrm{p}_i}\right)^{-1} \qquad \text{for species } i = \mathrm{O}_2 \tag{8}$$

where k_j is computed with Eq. (7) with the constants reported for $j = 5, 6, 7, 8$ in Table 1. The surface reaction rates calculated according to Eqs. (6) and (8) for varying wall temperature are reported in Fig.1(a). The total erosion rate of carbon due to the surface heterogeneous reactions is finally expressed as:

$$\dot{m}_{\mathrm{w}} = \dot{m}_{\mathrm{w},\mathrm{H_2O}} + \dot{m}_{\mathrm{w},\mathrm{CO_2}} + \dot{m}_{\mathrm{w},\mathrm{OH}} + \dot{m}_{\mathrm{w},\mathrm{O}} + \dot{m}_{\mathrm{w},\mathrm{O_2}} \tag{9}$$

In terms of energy absorbed (or released) by the surface reaction, it is worth noting that the reactions with H_2O, CO_2, and OH are characterized by a positive heat of reaction, which means that energy is absorbed when carbon is oxidized by one of these oxidizing species, whereas the reactions with O_2 and O are characterized by a negative heat of reaction, hence energy is released (see Fig.1(b)). Therefore, the net amount of energy absorbed or even released by the

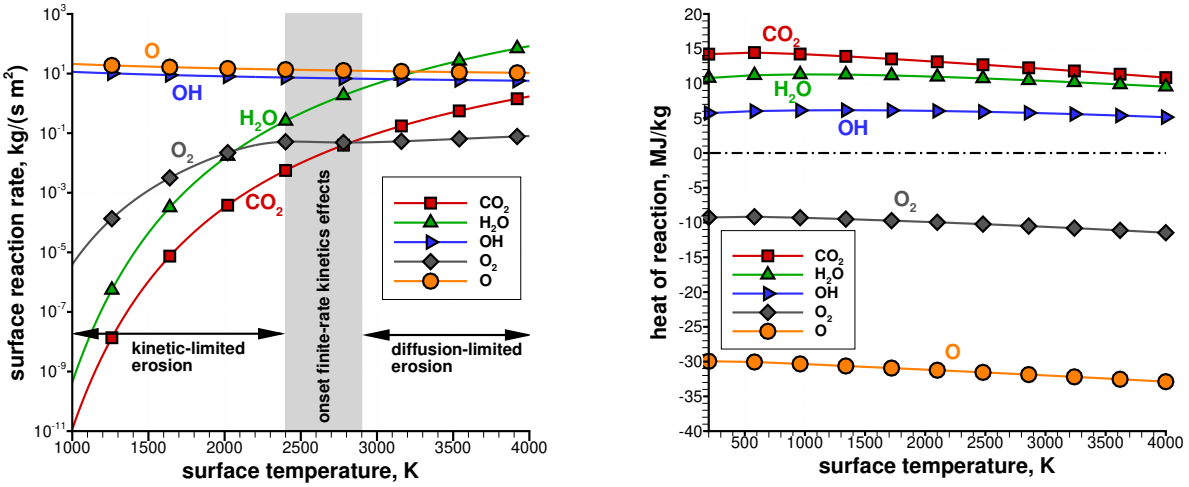

(a) Surface reaction rate at 1 atm.

(b) Heat of reaction per mass of graphite consumed.

Figure 1 Surface reaction rate and heat of reaction of heterogeneous surface reactions.

surface ablation process is strongly dependent on the chemical composition of the exhaust gases, due to the competition between endothermic and exothermic surface reactions.

In the present work, a unitary combustion efficiency has been considered in all the CFD simulations performed. The assumption of a unitary combustion efficiency has been guided by important considerations regarding HRE behavior. In

particular, it is well known that the HRE flow evolution inside the combustion chamber strongly depends on injector configuration, solid grain geometry, and post-chamber length, determining the engine combustion efficiency and the flow conditions at nozzle entrance. In case of non-optimized configurations, combustion efficiency can be low, and flow conditions at nozzle entrance can be characterized by flow stratification and/or incomplete fuel/oxidizer burning and mixing [16]. Since it is practically impossible to take into account all the combined effects of combustion chamber design parameters on nozzle erosion with reasonable computational times, the main objective of this manuscript is to perform parametric ablative numerical simulations which are independent of the specific geometry and/or flow conditions in the combustion chamber (i.e., injector, grain design, post-chamber size). This can be reasonably done only assuming that the combustion chamber design ensures a sufficiently good mixing and complete combustion, leading to a unitary combustion efficiency, meaning that flow conditions at nozzle inlet are independent of the evolution of the flow in the combustion chamber. Therefore, only the nozzle portion of the engine is simulated, reducing the computational efforts required in the parametric analysis, and the flow is assumed to be chemically inert (i.e., $\dot{\omega}_i = 0$ in Eq. (1)), so that finite-rate reactions are confined to surface chemistry. Hence, the ablation products are not allowed to react with the exhaust gas species as they are diffusing across the boundary layer. Moreover, exhaust gases are assumed to be frozen in the expansion process. In the last part of the work, gas-phase reactions are instead included (i.e., $\dot{\omega}_i \neq 0$ in Eq. (1)) in order to asses the range of validity of the frozen flow approach. In fact, although literature studies [38, 39] show that the nozzle ablation process is rather independent of gas-phase reactions in the boundary layer for solid rocket motors, this may not be the case for hybrid rocket engines. Hybrid rockets, in fact, differently from solid rocket motors which are inherently fuel-rich in almost all conditions, can often operate under oxygen-rich conditions. Hence, volumetric gas-phase exothermic reactions of carbon monoxide, the major ablation product of graphite, with free oxygen available in the boundary layer for oxidizer-rich operating conditions, may have a non-negligible effect on the surface ablation process. This aspect will be discussed in more details in Sec. VI.

C. Transient heat conduction

In the material response code employed in this work it is assumed that heat conduction into the graphite nozzle material is dominant in the direction normal to the local surface. In fact, although tangential temperature gradients exist along the nozzle wall, they are generally small if compared to the heat conduction in the wall normal direction and represent a second-order effect which has not been accounted for in the present analysis. In a moving local coordinate system tied to the receding surface, the temperature distribution for a non-decomposing material such as graphite is governed by the following equation:

$$\rho_s \frac{\partial h_s}{\partial t} = \frac{1}{A}\frac{\partial}{\partial \eta}\left(k_s A \frac{\partial T}{\partial \eta}\right) - \rho_s \dot{r}\frac{\partial h_s}{\partial \eta} \tag{10}$$

where $h_s(T) = \int c_s(T)dT$. The terms in Eq. (10) represent, from left to right, the sensible energy accumulation, the net conduction, and the net energy convected as a consequence of coordinate motion. The specific heat c_s and thermal conductivity k_s of the nozzle protection materials may experience significant variations in the temperature range in which they usually operate and therefore, in Eq. (10), they are allowed to vary with temperature. The following laws are used in order to obtain the graphite material properties for varying temperature [18]:

$$k_s(T) = C_1\ T^{-0.6} \tag{11}$$

$$c_s(T) = C_2\ \ln(T/T_{\text{ref}}) - C_3 \tag{12}$$

where the temperature T is expressed in Kelvin, C_1 = 3712 W/(m·K$^{0.4}$), C_2 = 651 J/K, C_3 = 2877 J/K, and T_{ref} = 1 K. The adopted graphite is characterized by a bulk density, ρ_s, of 1850 kg/m^3.

III. Experimental test case and numerical set-up

In this work we consider a series of 100N-thrust class hybrid rocket static firing tests using nitrous oxide (N_2O) as oxidizer and high-density polyethylene (HDPE) as fuel [40]. Parametric numerical simulations are performed in order to analyze nozzle erosion behavior under different operating conditions.

A. Experimental test case

The experimental oxidizer-to-fuel mass ratio (O/F) and the throat recession time histories are obtained from indirect measurements, using a Nozzle Throat Reconstruction Technique (NTRT) [18, 41, 42]. Similarly, for the throat wall temperature and the in-depth temperature profiles, the Throat-Temperature Reconstruction Technique (TTRT) proposed in [43] is used. These two methods were shown to be a useful tool to perform low-cost firing tests of HREs, including throat erosion and heating effects, without the requirement of complex measurement devices.

The NTRT is built upon the governing equations and concepts of the reconstruction techniques originally introduced in [41] to reconstruct the nozzle throat radius and oxidizer-to-fuel mass ratio histories through data reduction of commonly measured experimental values, such as: (1) oxidizer mass flow rate; (2) chamber pressure; (3) thrust; (4) overall fuel mass consumed; and (5) final nozzle throat radius. The basic concept of NTRT is the estimation of the nozzle erosion by solving the 1D governing equations for compressible flow in converging-diverging ducts, in conjunction with the governing equations for rocket performance. Solutions obtained from the NTRT are independent of the nozzle material, and thus may be applied to any nozzle shape or material as long as the assumptions behind the governing equations are satisfied.

In this work, a large number of N_2O-HDPE firing tests is considered [40]. The nozzle geometries employed in the test campaign are all characterized by a throat radius of 2 mm, including two different divergent cone half-angles: 1.91

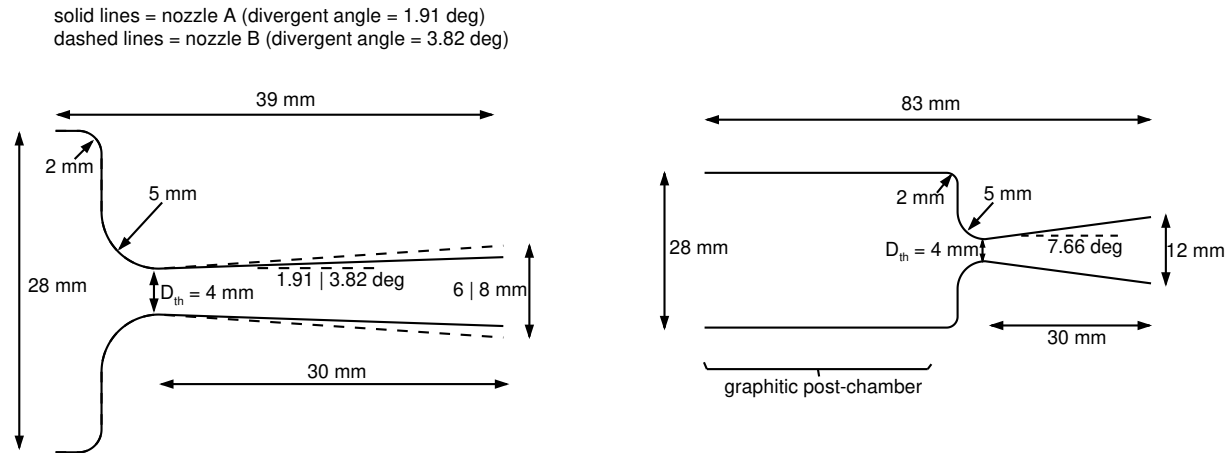

(a) Nozzle A and B.

(b) Nozzle C.

Figure 2 Schematics of the nozzles employed in the experimental campaign.

deg (nozzle A), and 3.82 deg (nozzle B). These conical nozzles are shown in Fig. 2(a). A third nozzle geometry is considered as well, including a long graphitic post-chamber and a divergent cone half-angle of 7.66 deg (nozzle C). This nozzle is shown in Fig. 2(b). The nozzle material used in all the experimental tests is graphite, for which properties are taken from the literature [18] and are reported in Sec. II.C.

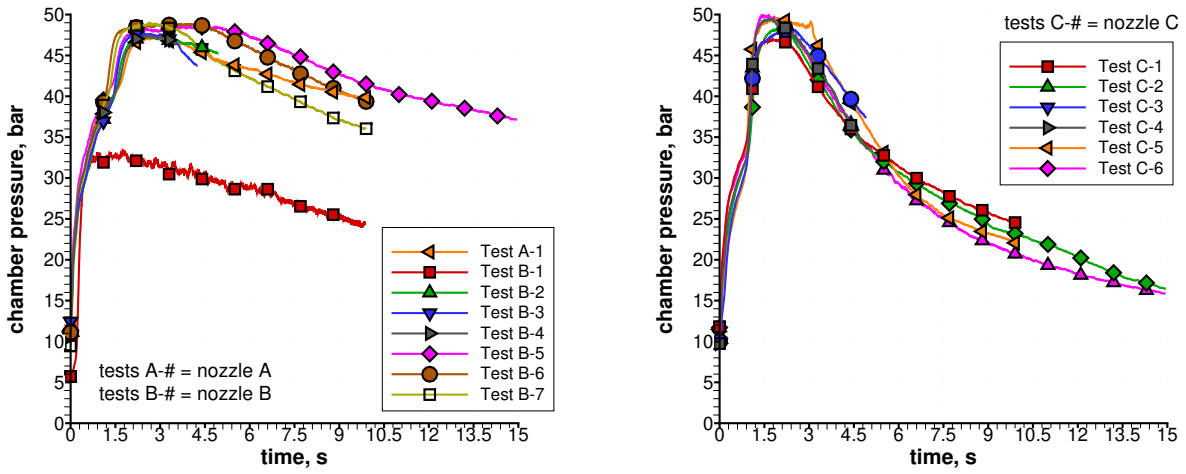

(a) Nozzle A and B.

(b) Nozzle C.

Figure 3 Experimental chamber pressure traces.

The most important measured and reconstructed internal ballistics parameters obtained by the NTRT for the test campaign analyzed are reported in Figs.3, 4, and 5. In particular, in Fig.3 chamber pressure traces obtained from direct

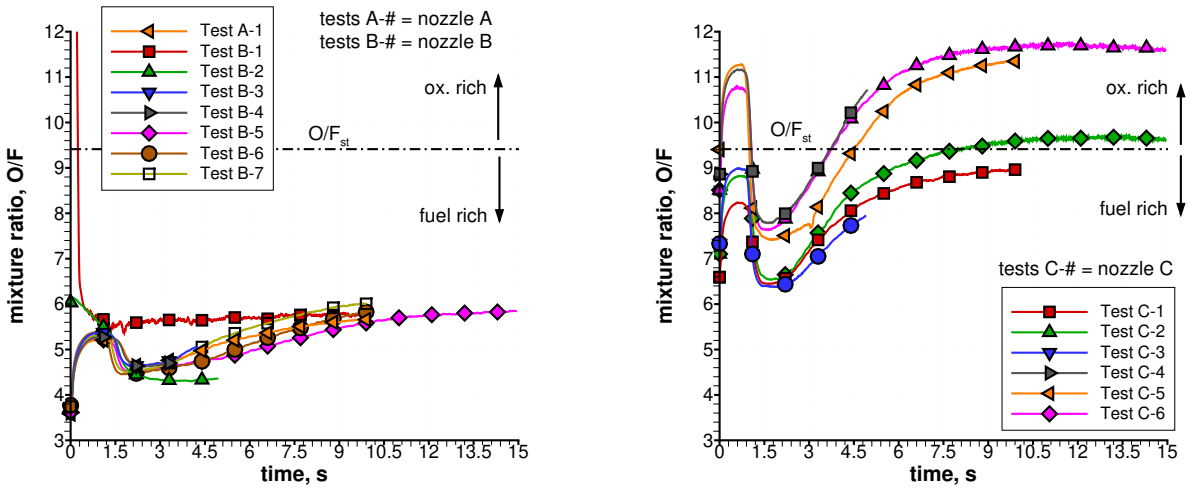

(a) Nozzle A and B.

(b) Nozzle C.

Figure 4 Experimental mixture ratio traces obtained by employing the NTRT reconstruction technique [40].

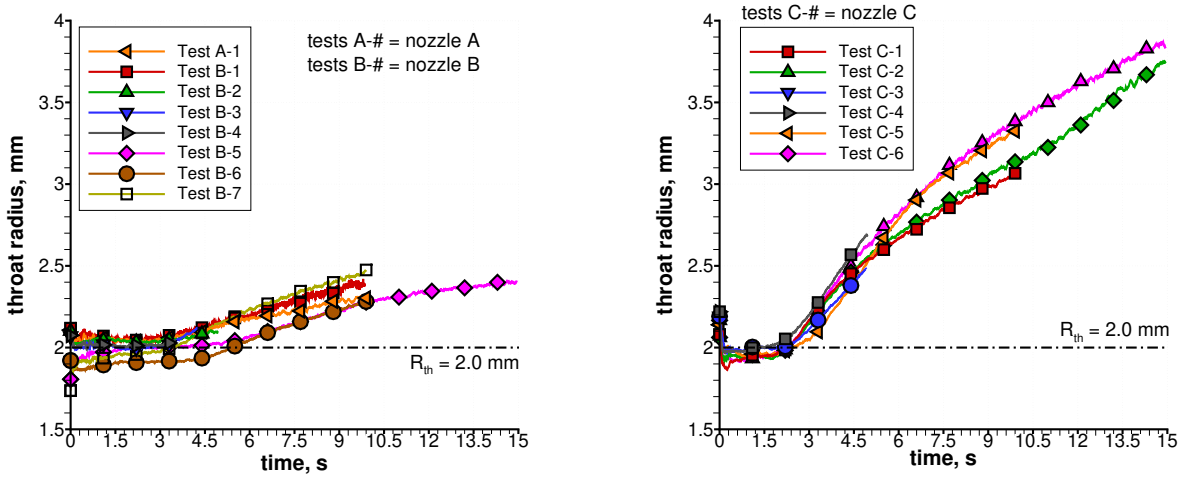

(a) Nozzle A and B.

(b) Nozzle C.

Figure 5 Experimental throat radius traces obtained by employing the NTRT reconstruction technique [40].

experimental measurements can be observed. It is worth noting how all firing tests are characterized by limited time durations, approximately of the order of 4 to 15 seconds, independently from the nozzle geometry employed. Measured chamber pressure values vary in the range 25 to 50 bar. Conversely to chamber pressures, mixture ratio evolutions over time for the tests analyzed (see Fig.4) have been obtained from indirect measurements, employing the NTRT. Those reconstructed mixture ratios are used here in order to estimate the average O/F for each firing test, which is needed in order to build up the test matrix for the numerical simulations. Firing tests employing nozzles A and B are characterized by fuel-rich conditions for the whole test duration (see Fig.4(a)), while firings using the nozzle C geometry

are characterized by close to stoichiometric conditions (see Fig.4(b)).

Table 2 Averages of directly measured experimental data (full test duration).

Test	t_b, s	t_{onset}, s	nozzle	D_{th0}, mm	p_c, bar	O/F	$\dot{r}$, mm/s	T_w, K	η_{c^*}
A-1	9.92	0.0	A	2.0	41.9 (±0.7%)	5.14 (±3.7%)	0.030 (±33.0%)	1498.3 (±9.7%)	0.83
B-1	9.85	0.0	B	2.0	28.5 (±1.0%)	5.95 (±31.4%)	0.040 (±25.9%)	1931.9 (±11.3%)	0.84
B-2	4.95	0.0	B	2.0	41.9 (±0.7%)	4.81 (±3.7%)	0.018 (±117.6%)	1513.1 (±9.6%)	0.75
B-3	4.25	0.0	B	2.0	41.3 (±0.7%)	4.91 (±3.5%)	0.028 (±85.7%)	1447.5 (±10.1%)	0.69
B-4	3.50	0.0	B	2.0	40.6 (±0.7%)	4.88 (±3.5%)	0.018 (±129.4%)	1131.6 (±9.0%)	0.67
B-5	14.95	0.0	B	2.0	42.7 (±0.7%)	5.21 (±3.8%)	0.027 (±25.5%)	1512.0 (±8.1%)	0.88
B-6	9.94	0.0	B	2.0	43.8 (±0.6%)	5.06 (±4.0%)	0.029 (±37.4%)	1520.6 (±7.1%)	0.78
B-7	9.90	0.0	B	2.0	41.5 (±0.7%)	5.24 (±3.6%)	0.048 (±21.9%)	1893.9 (±6.6%)	0.81
C-1	9.93	0.0	C	2.0	33.9 (±0.8%)	8.03 (±3.2%)	0.107 (±10.1%)	1960.9 (±7.6%)	0.81
C-2	14.95	0.0	C	2.0	28.7 (±1.0%)	8.82 (±3.1%)	0.117 (±6.2%)	1975.2 (±12.1%)	0.81
C-3	4.91	0.0	C	2.0	40.3 (±0.7%)	7.39 (±3.7%)	0.098 (±21.8%)	1664.6 (±16.1%)	0.74
C-4	4.97	0.0	C	2.0	40.1 (±0.7%)	9.35 (±3.3%)	0.139 (±15.5%)	1720.3 (±8.1%)	0.77
C-5	9.93	0.0	C	2.0	34.1 (±0.8%)	9.81 (±3.3%)	0.135 (±7.5%)	1981.3 (±9.0%)	0.84
C-6	14.94	0.0	C	2.0	28.0 (±1.0%)	10.67 (±2.9%)	0.123 (±5.5%)	1590.3 (±4.9%)	0.84

The most important information obtained from the NTRT is the time evolution of the nozzle throat radius, here shown in Fig.5. With the exception of the transient period during start-up, the results of NTRT agree closely with the measured values of the initial throat radius (note that the final throat radius is an input in the rebuilding technique), and display physically consistent (i.e., continuous and increasing) values of nozzle-throat erosion.

In order to define a numerical test matrix, the NTRT experimental data just presented have been manipulated according to two different criteria, as already done in a previous work by the authors [7]. The first criterion relies only on the directly measured experimental data, used in order to get the full test duration averaged parameters, here reported in Tab.2. In particular, in this case, average O/F values come directly from the knowledge of the overall oxidizer and fuel masses consumed. Moreover, the average nozzle-throat erosion rates are simply evaluated from the knowledge of the initial and final throat radius and the overall burning times. However, with this approach the solid transient heating is not accounted for, leading to possible underestimations of the erosion rates especially in the case of short duration firing tests. Hence, the second criterion relies on the identification of the instant when the nozzle erosion begins. This has been possible thanks to the NTRT reconstructed parameters, in particular by looking at the throat radius time histories. Later, once the throat erosion onset time has been identified, the initial throat radius has been always assumed to be equal to the measured initial radius, even if the NTRT can provide a slightly different value. Average oxidizer-to-fuel mass ratios have been determined in terms of mass flow rates integrals ratio by using the reconstructed O/F time histories and the measured oxidizer mass flow rates. The final average parameters obtained using this criterion (denoted as recession onset criterion) are summarized in Tab.3.

It is worth noting that average recession rates are always higher using the latter criterion, especially for firing tests

Table 3 Averages of experimental data obtained using the NTRT (recession onset).

Test	t_b, s	t_{onset}, s	nozzle	D_{th0}, mm	p_c, bar	O/F	$\dot{r}$, mm/s	T_w, K	η_{c^*}
A-1	9.92	2.5	A	2.0	43.3 (±0.7%)	5.23 (±4.0%)	0.040 (±32.8%)	1983.9 (±8.8%)	0.91
B-1	9.85	2.5	B	2.0	28.3 (±1.0%)	5.70 (±33.3%)	0.054 (±26.1%)	2698.7 (±11.6%)	0.89
B-2	4.95	2.5	B	2.0	46.5 (±0.6%)	4.33 (±4.4%)	0.037 (±118.0%)	2126.9 (±10.0%)	0.92
B-3	4.25	2.5	B	2.0	46.3 (±0.6%)	4.80 (±4.2%)	0.069 (±85.8%)	2117.4 (±10.6%)	0.88
B-4	3.50	3.0	B	2.0	46.9 (±0.6%)	4.70 (±4.3%)	0.082 (±245.1%)	1852.7 (±9.8%)	0.90
B-5	14.95	3.0	B	2.0	43.1 (±0.7%)	5.33 (±4.1%)	0.034 (±25.6%)	1857.8 (±7.6%)	0.95
B-6	9.94	4.0	B	2.0	44.2 (±0.6%)	5.29 (±4.2%)	0.048 (±37.3%)	1888.3 (±6.6%)	0.87
B-7	9.90	3.0	B	2.0	41.8 (±0.7%)	5.46 (±3.8%)	0.069 (±21.9%)	2211.1 (±7.8%)	0.90
C-1	9.93	2.5	C	2.0	32.2 (±0.8%)	8.35 (±3.2%)	0.143 (±10.0%)	2434.5 (±9.2%)	0.88
C-2	14.95	2.0	C	2.0	27.7 (±1.0%)	9.02 (±3.1%)	0.135 (±6.1%)	2241.2 (±14.0%)	0.86
C-3	4.91	2.0	C	2.0	43.8 (±0.6%)	7.14 (±4.1%)	0.165 (±21.8%)	2255.2 (±18.9%)	0.92
C-4	4.97	1.5	C	2.0	43.0 (±0.7%)	9.00 (±3.7%)	0.199 (±15.5%)	2158.5 (±10.3%)	0.93
C-5	9.93	2.0	C	2.0	33.4 (±0.8%)	9.95 (±3.3%)	0.169 (±7.5%)	2507.3 (±10.7%)	0.92
C-6	14.94	2.0	C	2.0	26.4 (±1.1%)	10.92 (±2.9%)	0.142 (±5.6%)	1823.1 (±6.4%)	0.89

characterized by short burning times and long throat erosion onset times. Average chamber pressures and mixture ratios are varied accordingly. In both Table 2 and 3, experimental averages of the throat wall temperature are reported as well. These values have been evaluated from the TTRT data reported in [40], which are not shown here for briefness. The TTRT is based on temperature measurements (i.e., thermocouples data) taken within the nozzle throat during static firing tests and on the flow properties of the combustion gases passing through the nozzle [43]. In the reconstruction technique, the heat transfer at the nozzle throat is assumed to be one-dimensional, and radiative heat transfer is neglected. Both these assumptions are in line with the numerical approach employed in this work, making the comparison between experimental and numerical data more consistent. Finally, it is worth noting that both Table 2 and 3 indicate different average values of combustion efficiency, as it tends to increase during the burn. Hence, higher average combustion efficiencies are obtained when the recession onset criterion is selected.

B. Computational set-up and grid convergence

The basic graphite nozzle geometries used in the numerical simulations performed in this work are the ones shown in Fig. 2 and the test conditions of interest are those reported in Tables 2 and 3. All the computations performed solve the flowfield up to the wall, using a suitably small mesh dimension at the wall to provide a good resolution of the boundary layer. In particular, the minimum height of the cell adjacent to the wall is equal to $\approx 10^{-7}$ m at throat location in order for the resulting y^+ to be of the order of 1 or smaller. Boundary conditions other than the ablating ones are enforced as follows: total temperature, total pressure, flow direction and chemical composition at the nozzle inlet (subsonic inflow), no assigned conditions at the outflow (supersonic outlet), and axial symmetry (see Fig. 6). The numerical simulations assume frozen chemical composition in the flowfield. Combustion chamber conditions, used in

the subsonic inlet boundary, have been obtained with the Chemical Equilibrium with Applications (CEA) code [30] by varying chamber pressures and O/F over a certain range of interest. Ten species (CO, CO_2, H_2, H_2O, OH, H, O, O_2, NO, and N_2) have been considered for each equilibrium simulation as they constitute more than 99.9% of the total combustion gas mass for the N_2O-HDPE propellant combination analyzed here.

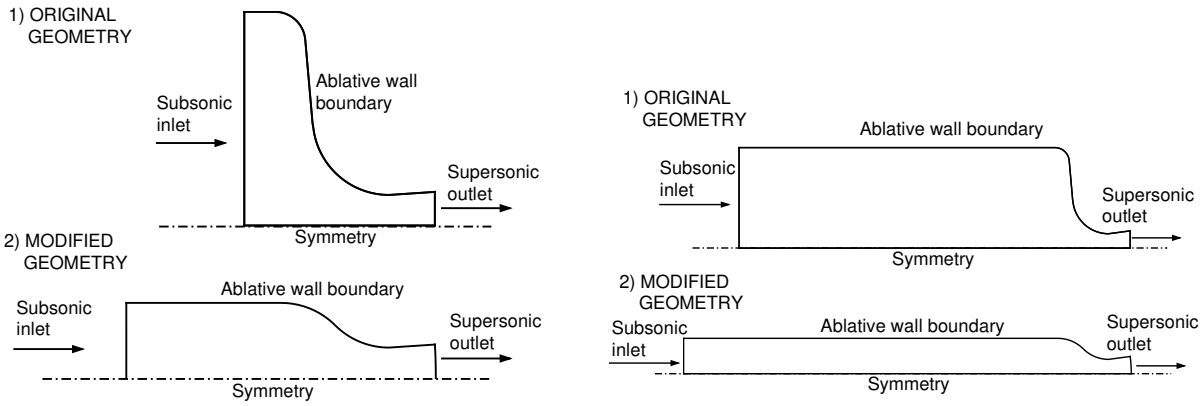

(a) Nozzle A and B.

(b) Nozzle C.

Figure 6 Schematics of the original and modified geometries with boundary conditions.

The original nozzle geometries have been slightly modified in the final numerical set-up adopted in this work (see Fig. 6). In addition to a divergent section cut-off, the convergent section has been modified, reproducing it by using two 45 deg circular arcs with the same 5 mm radius and with opposed curvature signs, so that it becomes parallel to the nozzle axis at the inlet section. A constant section portion has been then added prior the convergent zone, in order to keep the overall wall entrance length of the original nozzle. By applying these geometrical modifications, the modified nozzle geometries have the same throat to curvature radius ratio and the same wall entrance length of the original ones, hence no significant alterations on the throat ablative response are expected from numerical simulations. With this modified convergent shape arrangement, conformal mapping (employed by the CFD solver) can be efficiently applied to mesh the internal nozzle volume. The use of conformal mapping generates a grid that is well adapted to the geometry of the body, which can be of importance when wall parameters are sought for, such as in the present analysis.

The validity of the nozzle geometry modification just described has been checked by comparison with the numerical results carried out using the original geometry with an H-grid configuration (i.e. no conformal mapping and vertical grid lines). A reference pressure of 30 bar and the stoichiometric oxidizer-to-fuel mass ratio for the HDPE-N_2O propellant combination have been used. The main results obtained are summarized in Fig. 7. Concerning nozzle B, which is characterized by a short entrance length, differences in computed results between the two shapes are negligibly small at the throat location, hence the modified convergent shape nozzle profile has been used in the following analysis using only grids generated by conformal mapping. A similar result is foreseen for nozzle A, which convergent geometrical

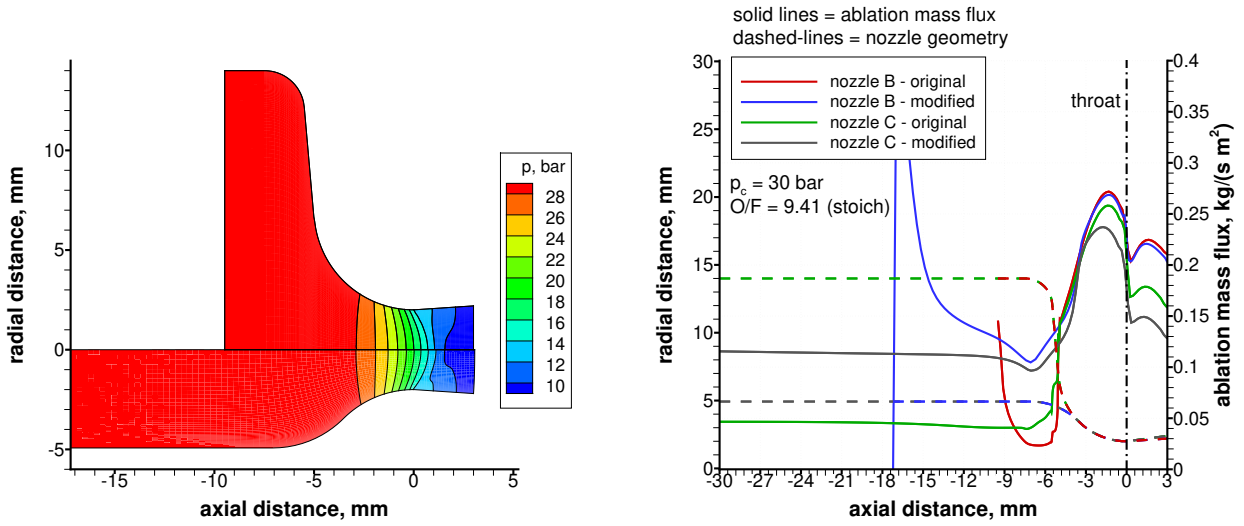

(a) Pressure flow fields for nozzle B.

(b) Ablation mass flux for nozzles B and C.

Figure 7 Effects of the nozzle geometry modifications on the pressure flow-field and throat ablation mass flux.

characteristics are the same as nozzle B (see Fig.2). Conversely, concerning nozzle C, which is characterized by a longer entrance length than nozzle A and B, there are substantial differences in the throat ablation mass flux considering the original and modified nozzle shape (see Fig.7(b)). In particular, throat ablation mass flux is lower for the modified geometry. The reason is the higher velocity (i.e., different Reynolds number) of the flow in the long modified convergent region, which leads to a greater development of the boundary layer than in the original nozzle, characterized by a higher contraction ratio (i.e., a lower flow velocity in this region and a slower boundary layer development). This is affecting the ablation mass flux at throat location. As shown in Fig.7(b), throat ablation mass flux for the original nozzle C geometry is more in line with the modified nozzle B one, with just a 7% difference, even if the entrance lengths are very different. For this reason, in the following, results from the nozzle B modified convergent geometry, using conformal mapping, have been assumed as representative of the original nozzle C convergent geometry as well, as in this particular case the long entrance has shown to have a limited effect (i.e., only 7% reduction) on the throat ablation mass flux.

The different divergent angles of the experimental campaign analyzed (see Fig.2) have been investigated looking at possible effects on the throat ablation mass flux. The results obtained are shown in Fig.8. As evident, variations of the nozzle divergent geometry have a negligible effect on the throat ablation mass flux, just altering the numerical results in the divergent portion of the nozzle. For this reason, from now on, a single nozzle geometry will be numerically analyzed (i.e., modified nozzle B), as the throat ablation mass flux is the main quantity which is sought for in this work.

The numerical solutions have been verified by a grid convergence analysis on three grid levels. Each finer mesh has been obtained by doubling the number of nodes in each coordinate direction starting from the immediately coarser mesh level, resulting in 2000, 8000, and 32000 points for the coarse, medium, and fine mesh respectively. From the numerical

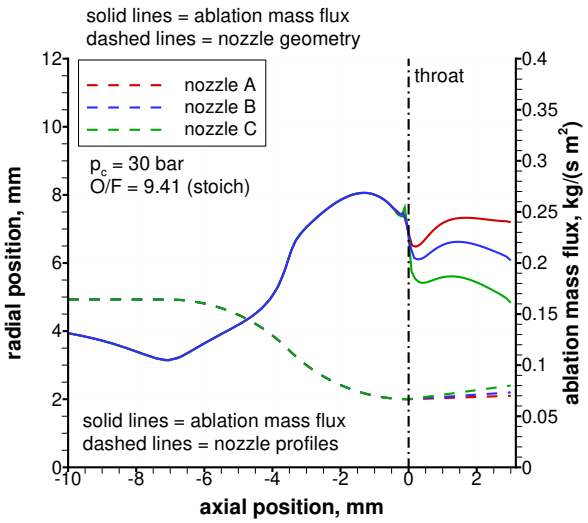

Figure 8 Effects of the nozzle divergent angle on the ablation mass flux distribution along the nozzle length.

solutions on the aforementioned three grid levels it is possible to compute the order of convergence, the correspondent Richardson-extrapolated solution [44, 45], and the relative numerical error as:

$$n = \frac{1}{\ln(m)} \ln\left(\frac{f_{\text{medium}} - f_{\text{coarse}}}{f_{\text{fine}} - f_{\text{medium}}} \right) \tag{13}$$

$$f_{\text{RE}} = \frac{f_{\text{medium}}^2 - f_{\text{fine}} f_{\text{coarse}}}{2 f_{\text{medium}} - f_{\text{fine}} - f_{\text{coarse}}}, \qquad \varepsilon = \frac{| f - f_{\text{RE}} |}{f_{\text{RE}}} \tag{14}$$

where $L_{\text{coarse}} = m L_{\text{medium}} = m^2 L_{\text{fine}}$, hence $m = 2$. Figure 9 shows that the numerical errors of the wall temperature and ablation mass flux at throat always decrease as the spatial resolution grows, with a convergence order higher than the theoretical second order. In particular, the numerical error with respect to the Richardson-extrapolated solution of the medium-level solution is practically always below 3%. Therefore, the medium-level grid is considered sufficiently refined for the present analysis.

IV. Steady-state CFD results

The CFD model described in the preceding sections is used here to simulate the nozzle erosion in HRE environments employing the N_2O-HDPE propellant combination. The final purpose is to perform an extensive parametric numerical analysis, including the effect of different operating conditions (i.e., chamber pressure and O/F ratio). A similar analysis has been also performed in a previous work by the authors concerning the LOX-HDPE propellant combination and employing different motor firings [7].

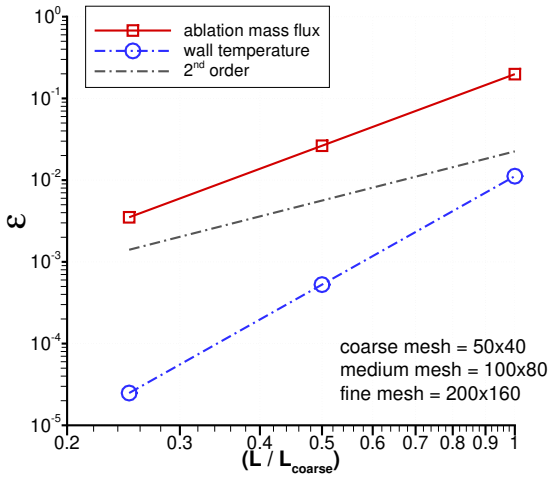

Figure 9 Grid convergence analysis for the modified nozzle B geometry considering the throat solution (L is the grid characteristic length).

A. Oxidizing species contribution

Firstly, a preliminary numerical analysis has been carried out in order to understand how the different oxidizing species contribute to the overall ablation mass flux by varying the oxidizer-to-fuel mass ratio at a reference pressure of 30 bar. At fuel-rich conditions (i.e., O/F=4.7), water vapor is the dominant oxidizing species, contributing to almost 95% of the total throat ablation mass flux (see Fig.10(a)). This is related to the high reaction rate of water vapour at high temperatures (see Fig.1(a)) and its abundance in the combustion gas composition at fuel-rich O/F (see Fig.11(a)). Regarding stoichiometric conditions (i.e., O/F=9.41), water vapor contribution is reduced from 95% to approximately 66% of the total throat ablation mass flux (see Fig. 10(b)). Moreover, OH is the second most important oxidizing species, with an increased contribution to the overall ablation with respect to fuel-rich conditions (18% at O/F=9.41 vs. 2.5% at O/F=4.7). At stoichiometric conditions, non-negligible contributions also come from molecular and atomic oxygen. CO_2 in instead not able to contribute significantly to the overall erosion even if present in large quantities (see Fig. 11(a)) due to its low reaction rate (see Fig. 1(a)). Lastly, at oxidizer-rich conditions (i.e., O/F=31.38), the water vapor contribution to the overall ablation mass flux is further reduced to approximately 41% (see Fig. 10(c)). An important difference with respect to fuel-rich and stoichiometric conditions is that the most important oxidizing species is now molecular oxygen O_2, with a contribution to the overall ablation mass flux similar to water vapor (i.e., 46%). This is related to the abundance of O_2 in the combustion gases moving towards oxidizer-rich conditions (see Fig.11(a)). The oxidizing species (and consequently, the thermochemical ablation reaction) governing nozzle ablation at varying O/F exhibits a significant influence on the overall ablation process. Indeed, reactions in Table 1 are characterized by different reaction heats (see Fig.1(b), which determine the energy to be more absorbed or more released at wall. In this context, it is worth noting how in case of O and O_2, ablation reactions are characterized by a negative reaction heat (i.e.,

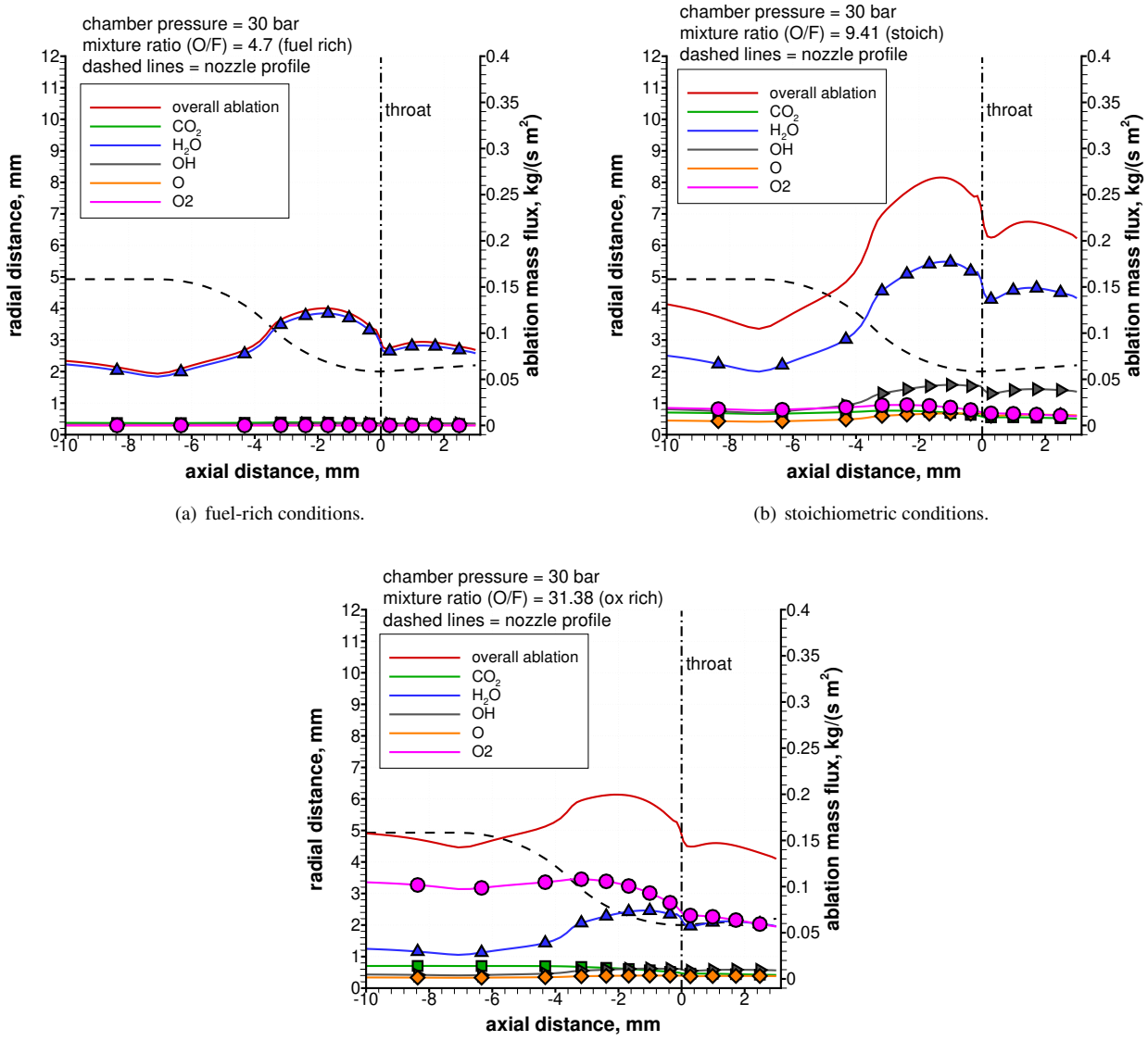

(a) fuel-rich conditions.

(b) stoichiometric conditions.

(c) oxidizer-rich conditions.

Figure 10 Contributions to the overall ablation mass flux from the different oxidizing species for different mixture ratios for the N_2O-HDPE propellant combination.

energy is released). Consequently, under oxidizer-rich conditions, the ablative process (guided by O_2) is less capable of absorbing energy than in case of stoichiometric and fuel-rich conditions, leading to generally high wall temperatures. This aspect will be crucial in the understanding of the throat erosion rate and throat wall temperature trends obtained in the following of this work by performing parametric numerical simulations of nozzle heating and erosion at varying mixture ratio.

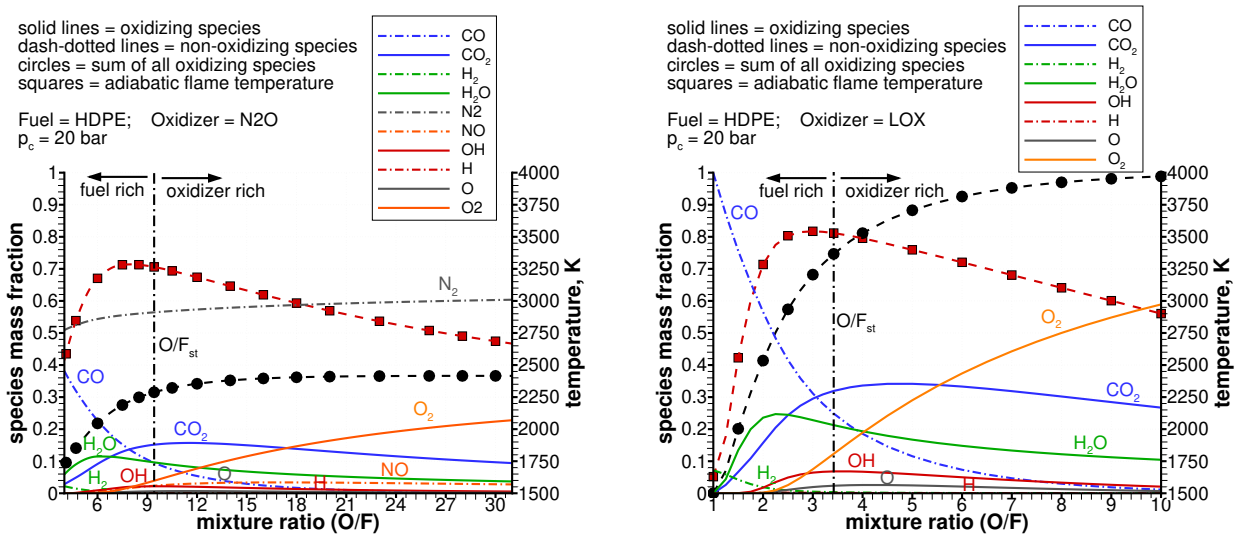

(a) N_2O-HDPE.

(b) LOX-HDPE.

Figure 11 Flame temperature and combustion gas composition at varying mixture ratios for both N_2O-HDPE (left) and LOX-HDPE (right) propellant compositions according to chemical equilibrium calculations [30].

B. Mixture ratio, pressure, and oxidizer effects

In HRE applications, it is important to investigate the combined effect of chamber pressure and mixture ratio on the nozzle throat erosion due to the possible O/F shift during both steady-state operation and throttling (see Fig.12). As expected, throat ablation mass flux grows with a power law with chamber pressure in the range obtained during the experimental campaign under investigation (10 to 50 bar, see Fig.12(a)). This is a typical result for nozzle throat ablation [6, 7, 20], and a direct consequence of the Bartz law [46]. However, the pressure exponent decreases moving towards oxidizer-rich conditions, where it is reduced approximately by 12% with respect to the stoichiometric one, underlining a mutual dependence for nozzle throat ablation on chamber pressure and mixture ratio. Concerning mixture ratio dependence, in the range from O/F=3.76 to 31.38 (i.e., equivalence ratios ϕ=2.5 to 0.3), the throat ablation mass flux peaks at slightly oxidizer-rich condition (Fig.12(b)). It is interesting to note that the throat ablation is only slightly reduced moving from stoichiometric towards oxidizer-rich conditions (especially at low pressures), while it is strongly reduced in the fuel-rich region. These results are a direct consequence of the particular oxidizing species guiding ablation at varying O/F, and are also associated to the wall temperature behavior, as discussed later.

The results above are consistent with the ones obtained with the HDPE-LOX propellant combination in a previous work by the authors [7], indicating that the ablation phenomenon is qualitatively similar with different oxidizers. However, it is worth noting that the pressure exponents obtained in this work using nitrous oxide (see Fig.12(a)) are lower than those reported in [7] using oxygen. However, the nozzle geometries employed in this work and in [7] differ substantially in terms of scale (i.e., throat radius), entrance length, and contraction ratio. In order to clarify this difference in terms of pressure exponents, the nozzle geometry described in [7], characterized by the higher pressure

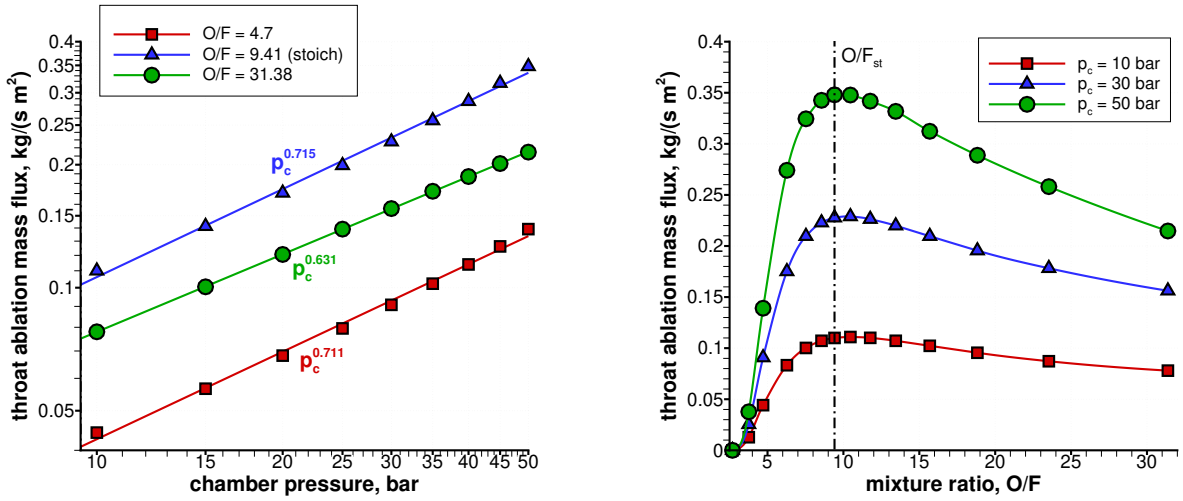

(a) log scale

(b) linear scale

Figure 12 Nozzle throat ablation mass flux distributions for different mixture ratios at varying chamber pressures (left) and for different chamber pressure at varying mixture ratios (right) for the N_2O-HDPE propellant combination.

exponent (see nozzle B3 schematic in Fig.13), is considered here as well with the HDPE-N_2O propellant combination. Results in case of both N_2O and LOX employing the nozzle B3 geometry depicted in Fig.13 are shown in Fig.14. Even

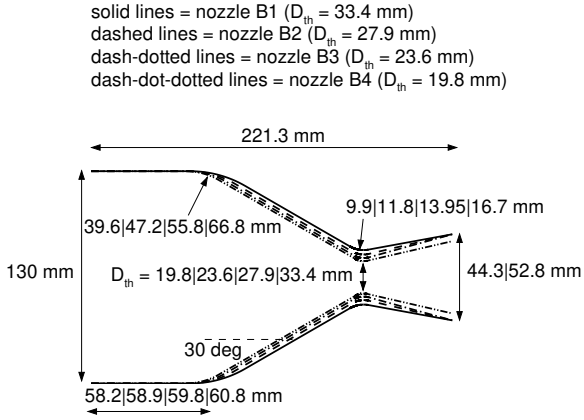

Figure 13 High contraction ratio nozzle schematics analyzed in [7] employing the HDPE-LOX propellant combination.

if mixture ratio values in Figs.14(a) and 14(b) are different, equivalence ratios are extremely similar, ensuring the validity of the numerical result comparison. The results obtained underline how the absolute value of the pressure exponent is mainly influenced by the nozzle geometry and not by the oxidizer. In fact, by changing only the nozzle geometry, the pressure exponent for the HDPE-N_2O propellant combination (see Fig.14(a)) is largely increased with respect to the one previously observed (see Fig.12(a)), reaching values similar to those obtained in [7] using oxygen (see

Fig.14(b)). However, the pressure exponent is decreased by 11.3% and 26.2% for nitrous oxide and oxygen, respectively,

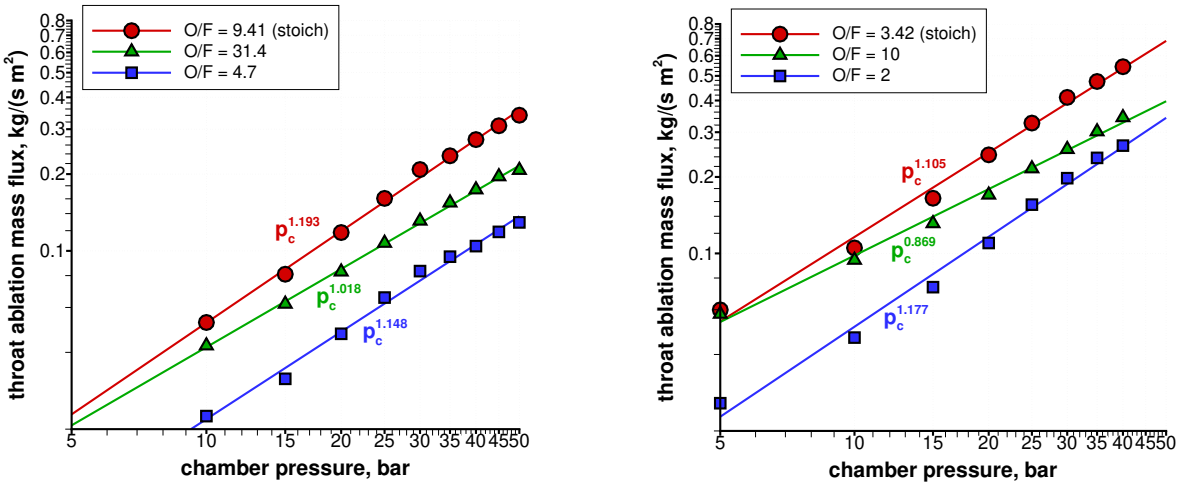

(a) N_2O-HDPE.

(b) LOX-HDPE [7].

Figure 14 Nozzle throat ablation mass flux distributions for different mixture ratios at varying chamber pressures (log scale) for both N_2O-HDPE (left) and LOX-HDPE (right) propellant combinations, computed on the nozzle geometry of [7].

moving from fuel-rich to oxidizer-rich conditions (see Fig.14). The fact that the pressure exponent is less reduced in the oxidizer-rich zone in case of nitrous oxide with respect to oxygen can be attributed to the different composition of the combustion gases (see Fig.11). In particular, in the case of nitrous oxide, the oxidizing species always represent less than 40% of the overall species, even in case of highly oxidizer-rich conditions. Conversely, oxidizing species cover almost 100% of the combustion gases at oxidizer-rich conditions in case of oxygen. The lower content of oxidizing species is expected to lead to lower ablation mass fluxes at the same operating conditions, as already reported in [5] and confirmed from the results shown in Fig.14. For the specific conditions in this work, nitrous oxide shows on average a 53% lower ablation mass flux than oxygen. Moreover, in case of the HDPE-N_2O propellant combination, the presence of a large quantity of molecular nitrogen at oxidizer-rich conditions is expected to influence the species diffusion process in the boundary layer as well, influencing the ablation process and leading to a different response of the throat ablation mass flux to chamber pressure variation with respect to the case of oxygen.

C. Throat wall temperature

The combined effects of varying chamber pressure and oxidizer-to-fuel mass ratio has been investigated also concerning throat wall temperature (see Fig.15). Pressure effects on throat wall temperature are not as evident as previously observed for throat ablation mass flux (see Fig.15(a)). The main reason is that chamber pressure only slightly affects flame temperatures, while it leaves practically unchanged the exhaust gas chemical composition. However, it

is worth noting that, depending on mixture ratio conditions, throat wall temperatures change with respect to flame temperatures (see Fig.15(b)). In particular, at oxidizer-rich mixture ratios, the throat wall temperature is still as high as at stoichiometric conditions, even if the flame temperature is considerably reduced. It is interesting that throat wall temperatures peak at oxidizer-rich conditions, as previously observed for the throat ablation mass flux, while flame temperatures peak at slightly fuel-rich conditions. This underlines that the nozzle heating and ablation process is not solely influenced by flame temperature, but is also greatly affected by chemical composition of the exhaust gas, in particular by the main chemical reaction (endothermic or exothermic) guiding the ablation process (see Figs.1(b) and 10). Moreover, throat wall temperature is shown to be only slightly influenced by mixture ratio in the oxidizer-rich zone, while it is strongly varying at fuel-rich conditions. The almost flat wall temperature behavior at varying mixture ratio in the oxidizer-rich zone is attributed to the continuous increase in the O_2 mass fraction in the combustion products (see Fig.11(a)). This increase induces a higher exothermic contribution in the overall thermochemical ablation process (see Fig.1(b)), counterbalancing the decrease in adiabatic flame temperature (see Fig.15(b)). Conversely, in the fuel-rich zone, temperature sharply decreases with O/F due to the significant drop in flame temperature, unopposed by any exothermic reaction contributions. Similar results have been reported in case of oxygen in [7]. Throat wall temperature results in Fig.15 justify throat ablation mass flux trends previously discussed looking at Fig.12.

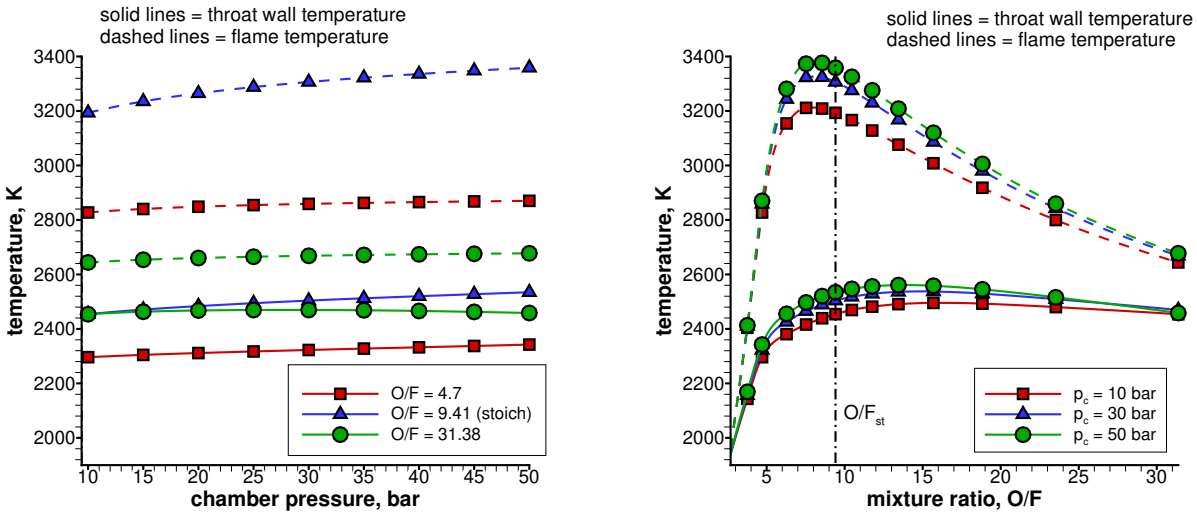

(a) linear scale

(b) linear scale

Figure 15 Adiabatic flame temperature and nozzle throat wall temperature distributions for different mixture ratios at varying chamber pressures (left) and for different chamber pressure at varying mixture ratios (right) for the N_2O-HDPE propellant combination.

D. Entrance length effect

Finally, an example of the effects of a different nozzle geometry on both throat ablation mass flux and throat wall temperature have been investigated by shortening the entrance length of the modified nozzle B (Fig.6). A nozzle

geometry characterized by a long entrance length leads to a lower throat ablation mass flux and to a flatter throat wall temperature distribution at varying mixture ratio in the oxidizer-rich zone, with a throat wall temperature maxima moved further in the oxidizer-rich zone. In fact, nozzle entrance length has a direct effect on boundary-layer development, altering boundary-layer-related phenomena, such as ablation. Similar results obtained with oxygen in [7] show that geometrical effects on throat ablation mass flux and throat wall temperature do not depend on the specific oxidizer.

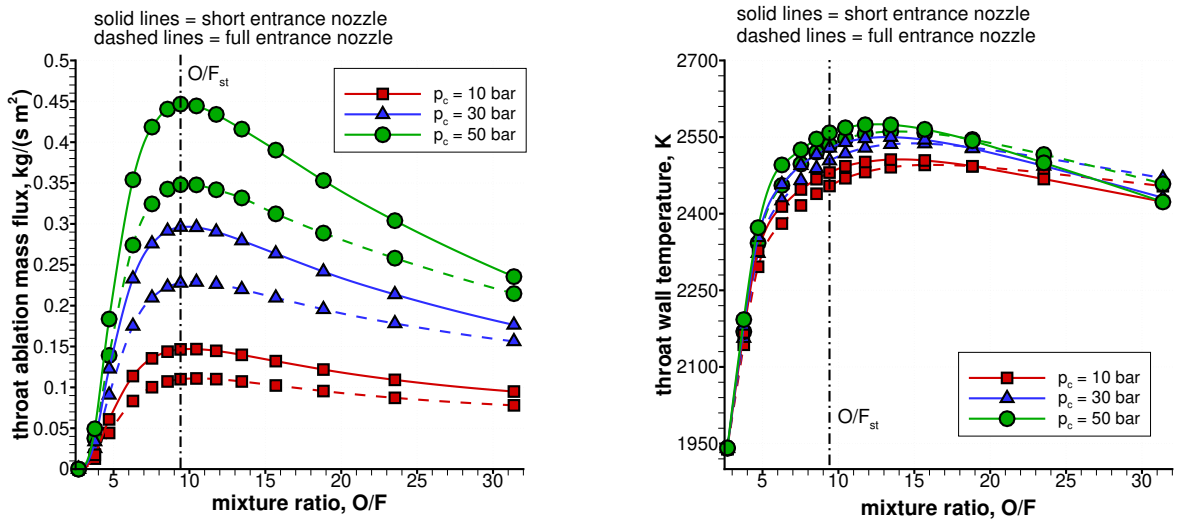

(a) Throat ablation mass flux.

(b) Throat wall temperature.

Figure 16 Effects of nozzle entrance length on throat ablation mass flux (right) and throat wall temperature (left) distributions for different chamber pressures at varying mixture ratio for N_2O-HDPE propellant combination.

E. Closed-form regression laws

Closed-form regression laws for nozzle throat ablation mass flux and throat wall temperature have been obtained for HDPE-N_2O following the same procedure thoroughly described in [7] starting from the parametric numerical analysis described in the previous sections:

$$\dot{m}_{w,th} = K_1 \; O/F^{-1.466} \; \exp^{\left(\frac{-19.82}{O/F} + 1.568\right)} \; p_c^{K_2 \; (0.0003627 \; O/F^2 \; - \; 0.01624 \; O/F \; + \; 0.8168)} \tag{15}$$

$$T_{w,th} = O/F^{-0.09096} \; \exp^{\left(\frac{-1.4}{O/F} + 8.135\right)} \; p_c^{\left(-\widetilde{K_1} \; 0.0001776 \; O/F \; + \widetilde{K_2} \; 0.01531 \; \right)} \tag{16}$$

where the parameters K_1, K_2, $\widetilde{K_1}$, and $\widetilde{K_2}$, which model geometrical effects, are considered here unitary since only one nozzle geometry has been analyzed. In case a different nozzle geometry has to be used, these parameters needs to be calibrated. The regressions in Eqs (15) and (16) successfully fit the numerical data, with a coefficient of determination R^2 above 0.98 for both nozzle throat ablation mass flux and throat wall temperature (Fig.17).

In [7], only the regression law for the ablation mass flux was shown. For completeness, the regression law for wall

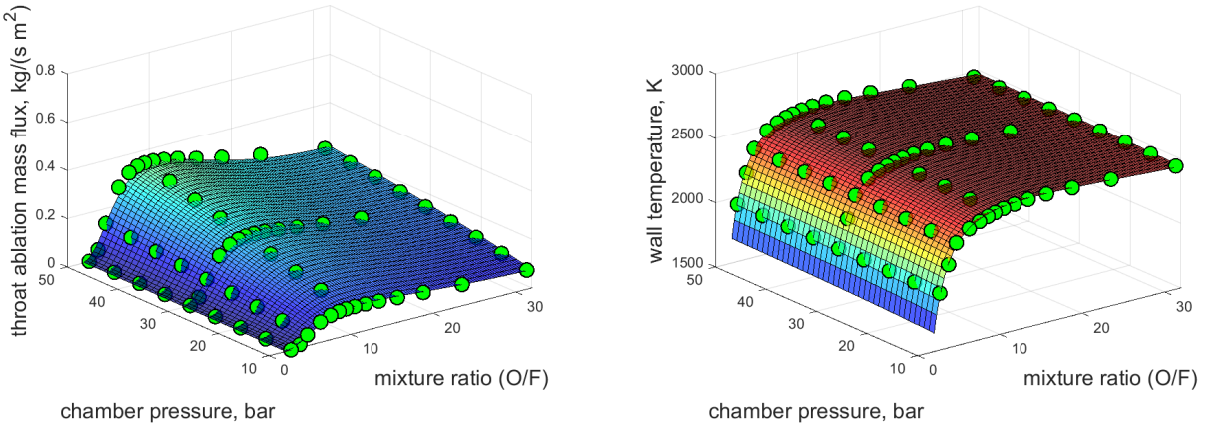

(a) Throat ablation mass flux.

(b) Throat wall temperature.

Figure 17 Fitting surfaces (Eqs (15) **and** (16)**) and numerical results (circles).**

temperature for the HDPE-LOX propellant combination is reported here:

$$T_{w,th} = O/F^{-0.08727}\ \exp^{\left(\frac{-0.6346}{O/F} + 8.027\right)}\ p_c^{\left(-\widetilde{K_1}\ 0.002814\ O/F\ +\widetilde{K_2}\ 0.03481\ \right)} \tag{17}$$

F. Comparison with experiments

A comparison between the closed-form regression law for the throat erosion rate with the experimental data of Tables 2 and 3 is presented in Fig.18. A tendency to overestimate the erosion rate for the full test duration experimental data is observed, especially at fuel-rich conditions (see Fig.18(a)). This is a combined effect of the transient heating phase, which is not accounted for in the CFD steady-state results used to derive the regression law, and of the low combustion efficiencies characterizing the full tests duration data, which range from 67% to 84% (see Table 2). The regression law performs better against the recession onset experimental data, capturing the nozzle throat erosion rate behavior at varying O/F (see Fig.18(b)). The transient heating phase is excluded from the average calculations for the recession onset data, and the combustion efficiencies are higher than in the full duration data, ranging from 86% to 95%.

However, the regression law results still overestimate most of the fuel-rich recession onset experimental data, possibly due to the reduced experimental combustion efficiency. In fact, CFD simulations have been carried out assuming a unitary combustion efficiency for all cases. On the other hand, moving towards stoichiometric conditions, the regression law underestimates the experimental results even if the experimental combustion efficiency is still sensibly lower than unity. A possible explanation of this underestimation can be the lack of modeling of gas-phase reactions effects. In fact, the assumption of frozen flow can be considered appropriate when low concentrations of O_2 are present in the combustion products, which is usually the case for composite solid propellants and, more generally, fuel-rich conditions. When this is not the case (higher O/F, see Fig.11), further oxidation reactions of the carbon monoxide and molecular

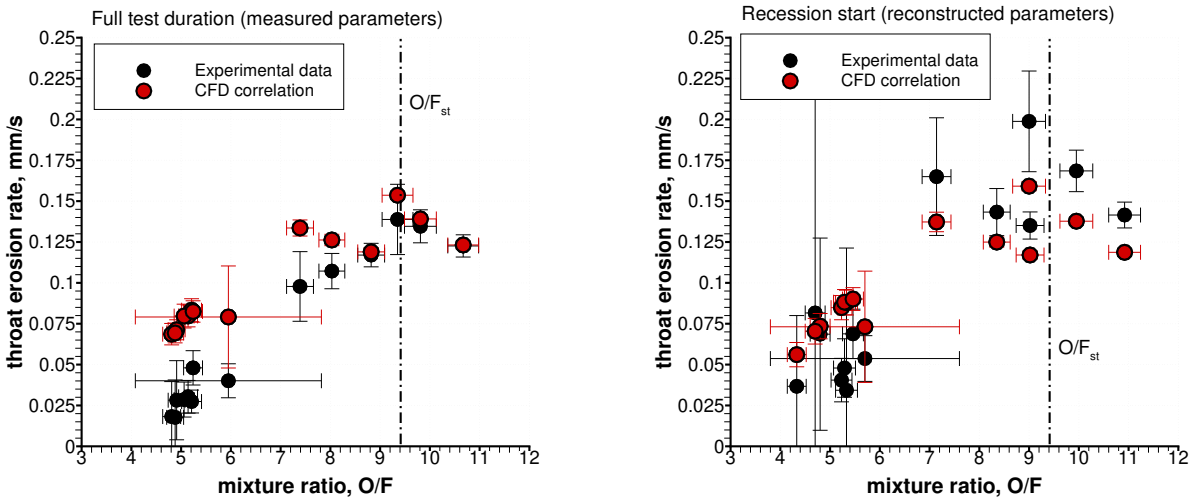

(a) Full test duration (Table 2).

(b) Recession onset (Table 3).

Figure 18 Comparison of CFD regression law with experimental throat erosion rates.

hydrogen produced by the ablation process may take place in the boundary layer, altering the composition and wall temperature.

The experimental average of the throat wall temperatures obtained through the TTRT technique [40] are compared to the numerical results in Fig.19. Throat wall temperatures are largely overestimated by the regression law for the full test duration data (see Fig.19(a)). This is somewhat expected, as the CFD simulations and the derived regression laws have been carried out assuming steady-state heat conduction, whereas the full test duration data includes the heating transient phase. On the other hand, by considering the recession onset time, the nozzle transient heating is almost completely neglected, and the time averages of the TTRT data are better approximated by the numerical throat wall temperatures at steady-state (Fig.19(b)). Finally, the agreement with the experimental data is further improved with respect to the recession onset data by considering only the last 0.5 seconds of the experiments (see Fig.19(a), as in this case the steady-state conditions can be assumed to be practically reached for most tests.

V. Transient solver results

In this section, a one-dimensional transient heat conduction solver is employed in order to analyze the in-depth heating of the nozzle thermal protection system (TPS). A complete validation of the transient heat conduction solver developed is reported in Appendix A.

The closed-form regression laws obtained from CFD steady-state computations performed in this work (i.e., Eqs. 15, 16, and 17) and in a previous work by the authors [7] have been used in order to get time-variable Dirichlet boundary condition in terms of wall temperature and erosion rate for the one-dimensional transient heating solver. The Dirichlet

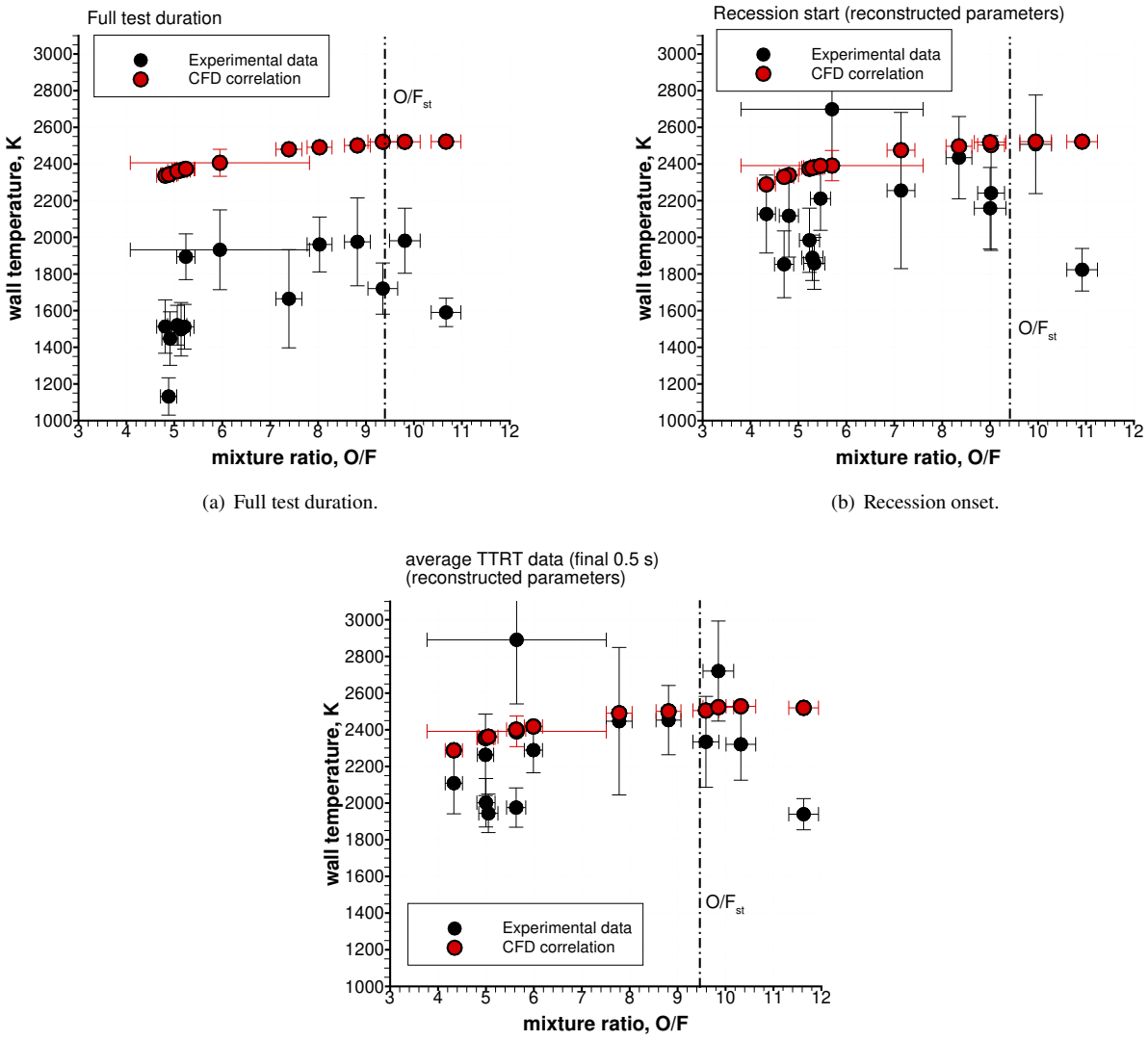

(a) Full test duration.

(b) Recession onset.

(c) Last 0.5 seconds.

Figure 19 Experimental throat wall temperature time-averages and CFD regression law data.

boundaries, applied to Eq.(10), write as follow:

$$T(x = 0, t) = T_{w,th}(t) \qquad (t = 0, ..., t_b) \tag{18}$$

$$\dot{r}(x = 0, t) = \dot{r}_{th}(t) \qquad (t = 0, ..., t_b) \tag{19}$$

where $\dot{r}_{th} = \dot{m}_{w,th}/\rho_s$, while $T_{w,th}$ and $\dot{m}_{w,th}$ are taken from the regression laws (see Eqs.(15), (16) and (17). The obtained results in terms of in-depth heating have been then compared to the available thermocouple data in order to prove the validity of the present numerical procedure. To this purpose, experimental traces of chamber pressure and

mixture ratio of both HDPE-LOX [7] and HDPE-N_2O tests have been considered. In particular, two different tests have been selected for each propellant combination: (i) tests B-1 and B-3 (taken from [7]) for HDPE-LOX; (ii) tests C-1 and C-3 for HDPE-N_2O (see Tables 2 and 3). For each propellant combination, the two considered tests employ the same engine configuration with different firing duration (approximately 4 s and 13 s for the HDPE-LOX tests B-1 and B-3 and approximately 10 s and 5 s for the HDPE-N_2O tests C-1 and C-3, respectively). A time step of 0.1 s has been selected for the boundary update in order to correctly capture the initial sudden rise of chamber pressure. A semi-infinite slab behavior is assumed in-depth, which is a valid assumption as long as the heating pulse is not able to reach the ablative material back-wall, and a planar coordinate system has been considered. Those hypotheses are in line with the assumptions made by the CFD code (i.e., one-dimensional heat conduction and infinite material thickness). Moreover, it is worth noting that the actual TPS thickness at throat is approximately 8.8 cm and 1.69 cm for the HDPE-LOX and HDPE-N_2O nozzles considered, respectively. A schematic of both LOX and N_2O nozzle TPS geometries, with details on boundary conditions and material layer thicknesses, is depicted in Fig.20.

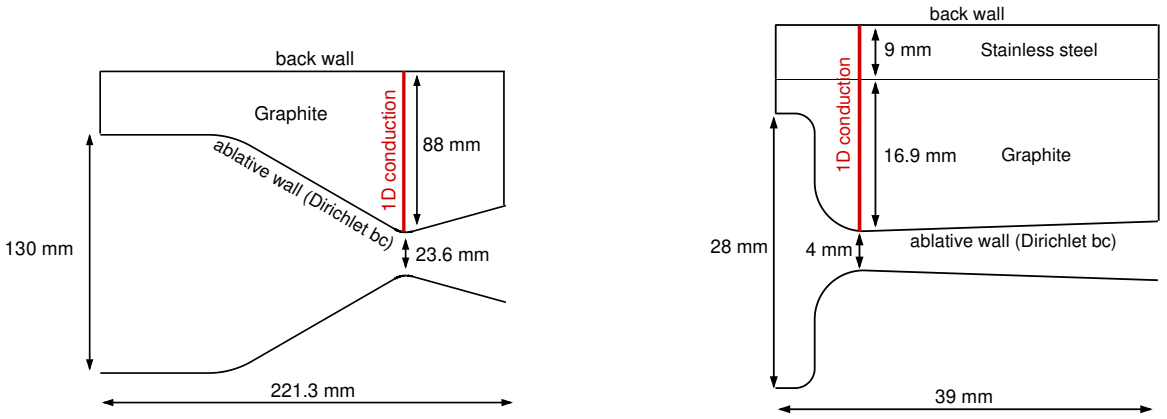

(a) HDPE-LOX nozzle.

(b) HDPE-N_2O nozzle.

Figure 20 Schematics of LOX and N_2O nozzle TPS with detail of section simulated by means of the 1D heat conduction solver (red line, i.e., throat section), boundary conditions, and material layers thicknesses.

The experimental traces of chamber pressure and mixture ratio of the HDPE-LOX tests B-1 and B-3 taken from [7] are reported in Fig.21(a). The corresponding throat wall temperature and erosion rate provided by the regression laws from [7] and Eq.17 (used as time-variable Dirichlet boundary conditions) are shown in Fig.21(b). Results obtained from the transient heating solver are summarized in Fig.22. In the first few seconds (i.e., from 0 to approximately 4 seconds), thermocouple data are overestimated by the numerical results for both tests, which is expected given the steady-state assumption of the regression laws. In fact, for short exposure times, the wall temperatures imposed at the surface are not representative of the actual values experienced by the nozzle. On the other hand, as the exposure time increases (i.e., approximately after 6 seconds, see Fig.22(b)), the numerical results start to be in good agreement with the available

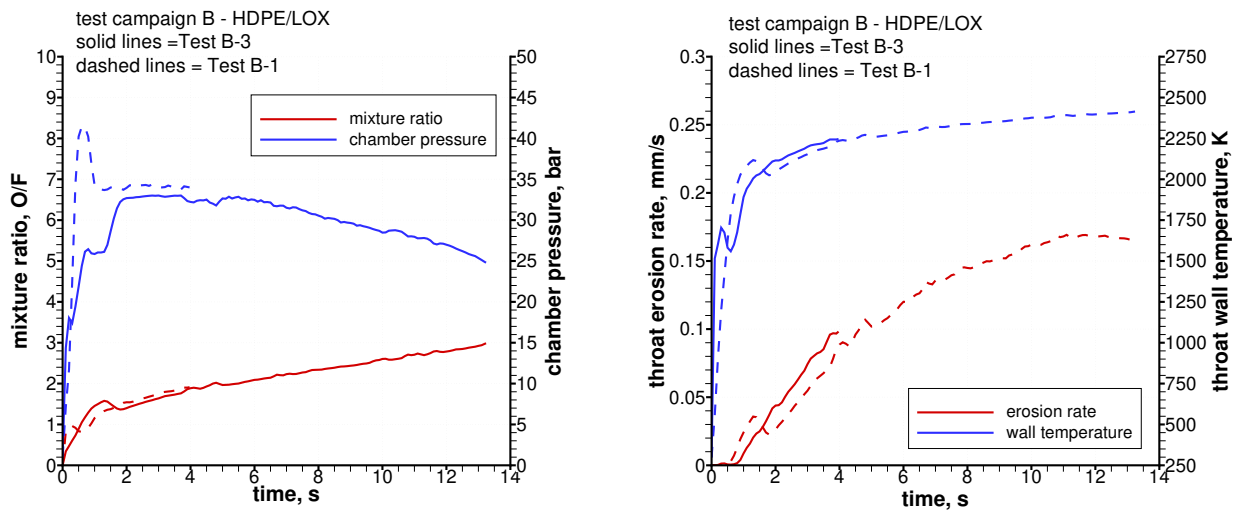

(a) Experimental traces.

(b) CFD correlations results.

Figure 21 Experimental traces from two engine firings in [7] using the HDPE-LOX propellant combination and correspondent throat erosion rate and wall temperature according to the CFD-derived regression laws (see [7] and Eq.17) employed as time-variable Dirichlet boundary conditions.

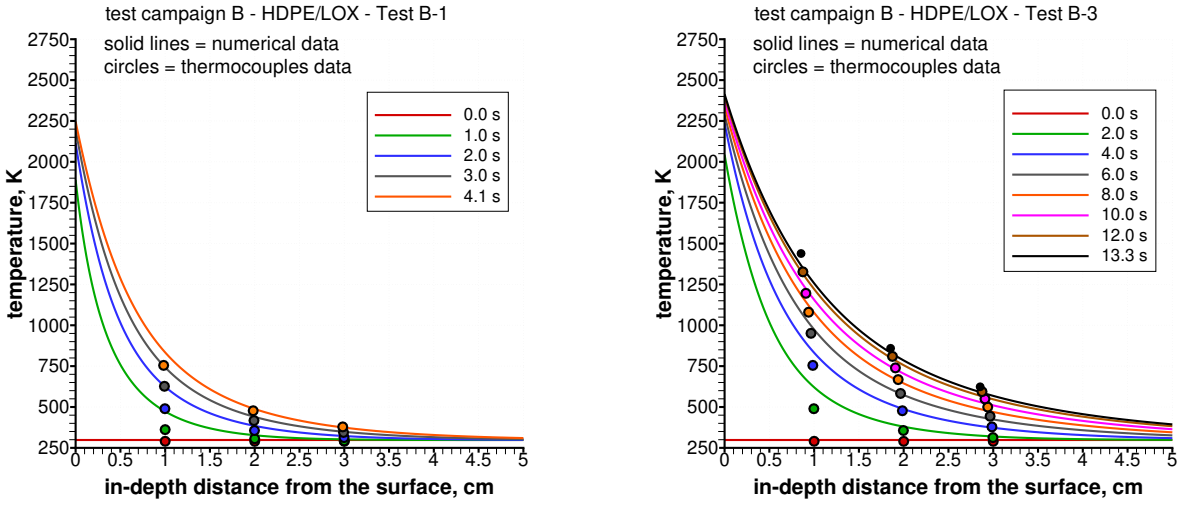

(a) Short duration test.

(b) Long duration test.

Figure 22 Comparison of the numerical results obtained from the transient heating solver against throat themocouples data for two firing tests in [7] using the HDPE-LOX propellant combination.

thermocouple data in terms of thermal penetration thickness (i.e., final temperatures at different distances from the surface) because steady-state conditions start to be approached. Finally, it is worth noting how the maximum heat penetration depth (with respect to the receding surface) for the two tests is approximately 5 cm, less than the overall TPS thickness at throat of 8.8 cm. Therefore, the heat wave is not able to reach the back of the TPS, justifying the adoption of a semi-infinite slab behavior in-depth.

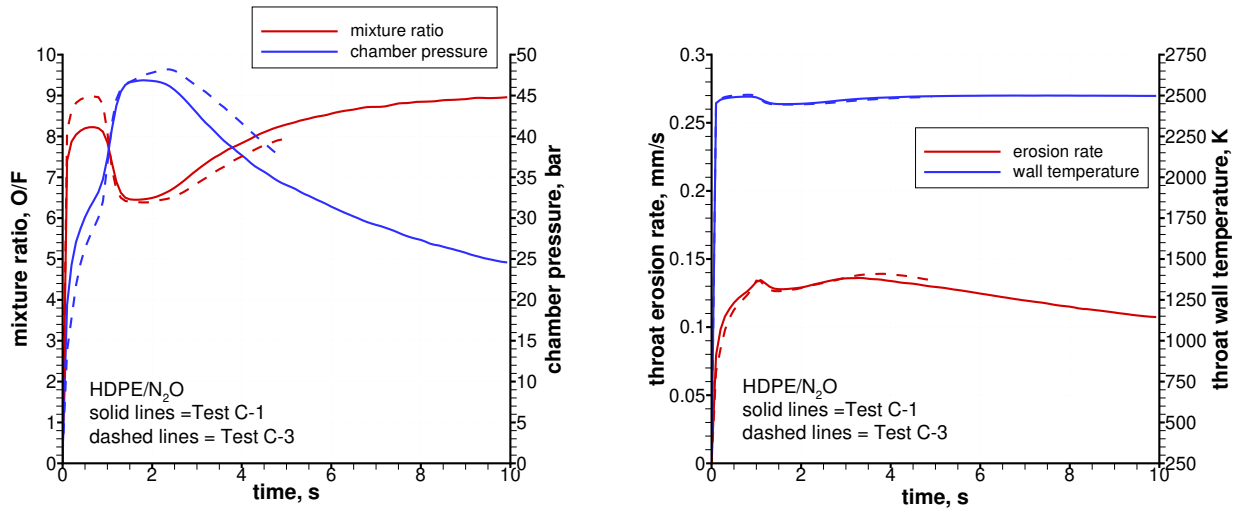

(a) Experimental traces.

(b) CFD correlations results.

Figure 23 Experimental traces of the HDPE-N_2O tests C-1 and C-3 (see Tables 2 and 3) and correspondent throat ablation and temperature according to the CFD-derived regression laws (Eqs.15 and 16) employed as time-variable Dirichlet boundary conditions.

The experimental traces of chamber pressure and mixture ratio of the HDPE-N_2O tests C-1 and C-3 have been reported in Fig.23(a). The corresponding throat wall temperature and erosion rate provided by the regression laws from Eqs. 15 and 16 (used as time-variable Dirichlet boundary conditions) are shown in Fig.23(b). Differently from the

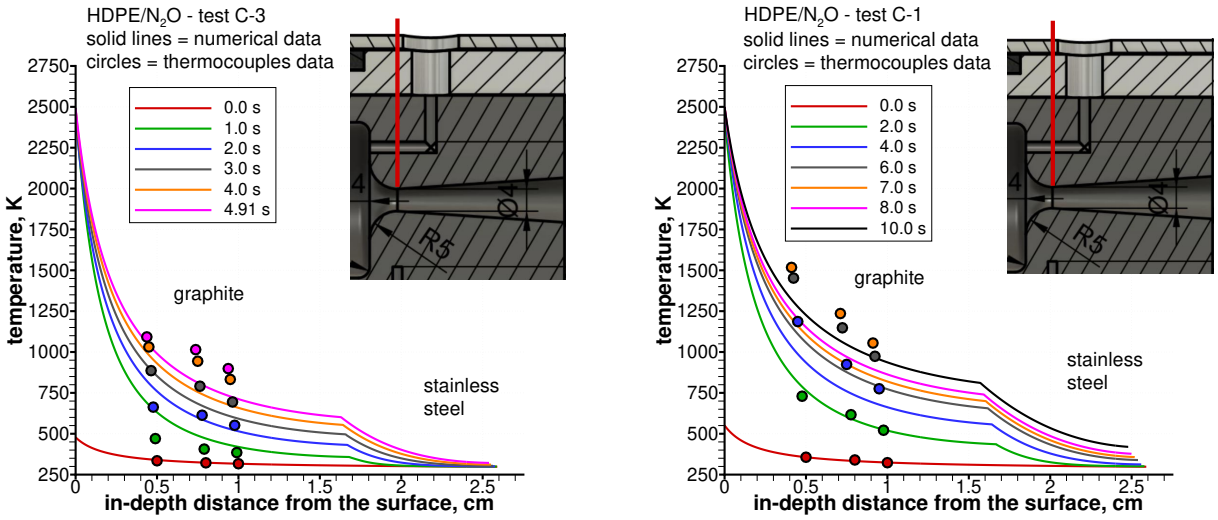

(a) Short duration test.

(b) Long duration test.

Figure 24 Comparison of the numerical results obtained from the transient heating solver against throat themocouples data for the selected firing tests using the HDPE-N_2O propellant combination including multi-material effects.

HDPE-LOX tests previously analyzed, for the HDPE-N_2O propellant combination the maximum heat penetration depth

(with respect to the receding surface) obtained for the two tests is greater than the overall TPS thickness at throat, which is 1.69 cm. Therefore, the interaction with the metallic structure underneath is foreseen, and multi-material effects shall be taken into account in the heat conduction solver. Moreover, the heat wave is now able to reach the back-wall, making the adoption of a semi-infinite slab behavior questionable for such tests. Therefore,a simple radiative boundary condition has been employed on the back-wall:

$$k_s \left.\frac{\partial T}{\partial \eta}\right|_{\eta=\eta_{end}} = \sigma\epsilon(T(\eta_{end})^4 - T_{amb}^4) \tag{20}$$

where η_{end} represents the coordinate on the ambient-side of the computational domain, T_{amb} is the ambient temperature, assumed to be 298.15 K, and ϵ is the surface emissivity, assumed equal to 0.9. Lastly, differently from HDPE-LOX propellant combination, for the HDPE-N_2O tests a cylindrical coordinate system has been employed in the transient heating solver. This has been deemed necessary due to the low throat radius of the nozzle (equal to 0.2 cm), which is more than one order of magnitude smaller than the overall thermal penetration thickness. On the other hand, for the HDPE-LOX tests, throat radius is of the same order of magnitude of the thermal penetration thickness, making the assumption of planar heat conduction more reasonable. Looking at the results obtained for the HDPE-N_2O tests in Fig.24, it is evident how, even if the qualitative behavior of the temperature profiles at varying time instants is correctly captured, thermocouples data are underestimated by the numerical solution. This can be explained considering possible multi-dimensional effects in the heat conduction process. In fact, nozzle curvature radius at throat is only 0.5 cm (i.e., much lower than the expected thermal penetration thickness), hence the heat waves coming from the nozzle convergent are expected to interact with the throat one, further increasing the temperature in-depth in this region (see the nozzle schematic detail reported in Fig.24). Moreover, it is worth noting that the CFD-derived closed-form regression laws employed in order to get the time-variable Dirichlet boundary conditions for the heating transient solver are affected by the hypothesis made in the CFD code. In particular, in the CFD ablative boundary condition, heat conduction is assumed to be one-dimensional, at steady-state, and a semi-infinite single-material slab behavior in-depth is considered. Therefore, if all these hypothesis are not respected, the present numerical approach can potentially lead to results inaccuracy.

Finally, the numerical approach proposed above can be employed for fast, inexpensive, and conservative preliminary evaluations of the thermal heating and penetration thickness of ablative thermal protections in HRE featuring long burn times. In order to improve the quality of the results in the early heating phase, a surface energy balance boundary condition in the heat conduction solver and a full transient coupling with the CFD solver should be employed. The same applies in order to take into account in the solid heat transfer modeling multi-material as well as multi-dimensional effects, which may become important in case of small nozzle dimensions. This comes however at a cost of increased complexity and computational time.

VI. Analysis of gas-phase reactions effects

As previously stated in Sec. IV.F, the assumption of frozen flow (made for the derivation of the regression laws in Sec.IV.E) is appropriate when low concentrations of O_2 are present in the combustion products, which is usually the case for fuel-rich and stoichiometric conditions. When this is not the case (i.e., high O/F), oxidation reactions of the carbon monoxide, CO, and molecular hydrogen, H_2, produced by the ablation process may take place in the oxy-rich boundary layer, altering the ablation process. In this section, the effects of the CO-H_2-O_2 gas-phase reactions on the nozzle throat erosion is analyzed by performing reacting numerical simulations. A reduced version of the CO-H_2-O_2 reaction mechanism proposed by Yetter et al. [47, 48] is employed, consisting of 10 species and 11 reactions (see Table 4). The original reaction mechanism, consisting of 14 species and 28 reactions [47, 48], has been reduced due to the absence of some species (i.e., Ar, HO_2, H_2O_2, and HCO) in the combustion products of the HDPE-LOX and HDPE-N_2O propellant combinations considered and to the low range of temperature (not relevant for rocket nozzle applications) over which the rate constant parameters of some reactions are provided. For the reactions in Table 4, the forward reaction rate, k_f, is expressed as:

$$k_{\mathrm{f},j} = A_j T^{n_j} \exp(-E_j/\Re T) \tag{21}$$

while the backward reaction rate, k_b, is calculated as:

$$k_{\mathrm{b},j} = k_{\mathrm{f},j}/K_j \tag{22}$$

where K_j is the equilibrium constant of the j-th reaction. The chemical source term of production/consumption of the i-th species is then evaluated with the law of mass action from the knowledge of the stoichiometric coefficients of reactants and products reported in Table 4.

Figure 25 shows the results obtained for a selection of the HDPE-LOX tests analyzed by the authors in a previous work [7] and for the HDPE-N_2O tests in Table 3. Frozen and reacting simulation results are compared in order to highlight gas-phase reaction effects on the ablation process. Regarding the HDPE-LOX tests (see Fig.25(a)), frozen and reacting simulations show similar results in the fuel-rich zone (i.e., left side of the plot). Non-negligible gas-phase reaction effects start to be notable approaching stoichiometric conditions. It is worth noting how in most of these almost-stoichiometric test cases the inclusion of the gas-phase reactions helps in improving the agreement with the experimental data. Then, moving towards oxidizer-rich conditions (i.e., right side of the plot), gas phase reaction effects yield throat erosion rates approximately 2 to 3 times higher than the corresponding frozen ones. It has to be underlined that for the two tests characterized by an O/F of approximately 6 (i.e., $\phi = 0.57$), the available experimental data are not considered completely reliable. In fact, these two tests had only a 3 bar chamber pressure difference [7]

Table 4 CO-H_2-O_2 gas-phase reaction mechanism [47, 48].

Reaction	j	A_j	E_j, kcal/mol	n_j	type
$H + O_2 \leftrightarrow O + OH$	1	$1.9 \cdot 10^{14}$	16.44	0.0	H_2-O_2 chain reaction
$O + H_2 \leftrightarrow H + OH$	2	$5.1 \cdot 10^{4}$	6.29	2.67	H_2-O_2 chain reaction
$OH + H_2 \leftrightarrow H + H_2O$	3	$2.1 \cdot 10^{8}$	3.43	1.51	H_2-O_2 chain reaction
$O + H_2O \leftrightarrow OH + OH$	4	$3.0 \cdot 10^{6}$	13.40	2.02	H_2-O_2 chain reaction
$H_2 + M \leftrightarrow H + H + M$	5	$4.6 \cdot 10^{19}$	104.38	-1.40	H_2-O_2 dissociation/recombination reaction
$O + O + M \leftrightarrow O_2 + M$	6	$6.2 \cdot 10^{15}$	0.0	-0.50	H_2-O_2 dissociation/recombination reaction
$O + H + M \leftrightarrow OH + M$	7	$4.7 \cdot 10^{18}$	0.0	-1.00	H_2-O_2 dissociation/recombination reaction
$H + OH + M \leftrightarrow H_2O + M$	8	$2.2 \cdot 10^{22}$	0.0	-2.00	H_2-O_2 dissociation/recombination reaction
$CO + O + M \leftrightarrow CO_2 + M$	9	$2.5 \cdot 10^{13}$	-4.54	0.0	Oxidation of CO
$CO + O_2 \leftrightarrow CO_2 + O$	10	$2.5 \cdot 10^{12}$	47.69	0.0	Oxidation of CO
$CO + OH \leftrightarrow CO_2 + H$	11	$1.5 \cdot 10^{7}$	-0.765	1.30	Oxidation of CO

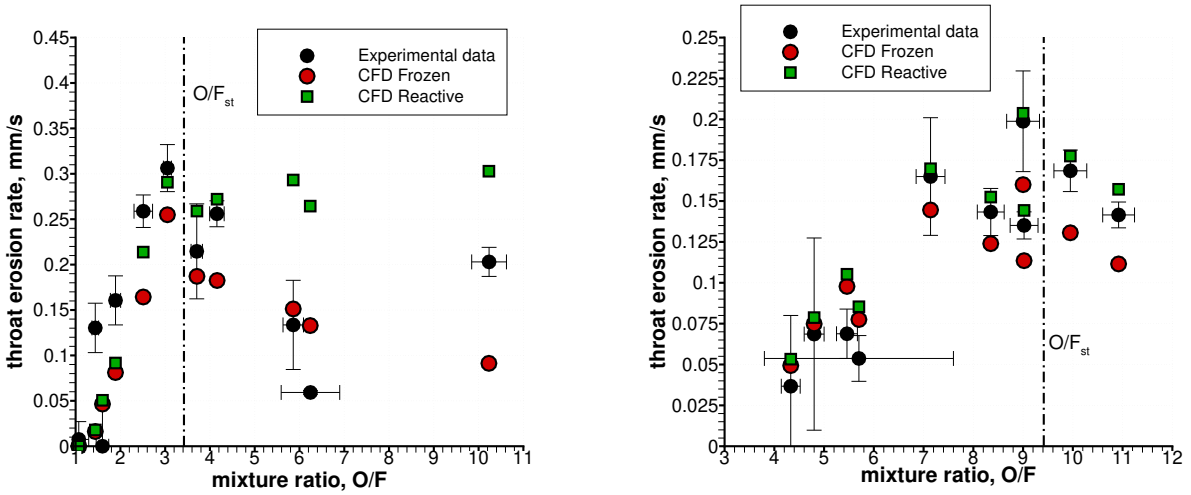

(a) HDPE-LOX tests [7].

(b) HDPE-N_2O tests.

Figure 25 Comparison of CFD data with experimental throat erosion rates for both HDPE-LOX and HDPE-N_2O propellant combination considering: (i) frozen chemical composition; (ii) gas-phase reactions.

(i.e., -19% for the lower chamber pressure one), which is not deemed sufficient to justify the experimentally observed deviation in terms of erosion rate (i.e., -53 %). Anyway, possible inconsistencies in the NTRT data may lead to a difficult interpretation of the experimental quantities especially in terms of average erosion rate when the reconstructed initial throat radius is not coincident with its measured value. This is the case of the two tests here considered, as shown in the NTRT data reported and described in [7]. Finally, regarding the most oxidizer-rich firing test, characterized by an O/F = 10.23 (i.e., ϕ = 0.33), the numerical throat erosion rate obtained with reactive simulations is more than 3 times the corresponding frozen one. In this case, the experimental erosion rate is in between the frozen and reactive numerical predictions. Further experimental data in the oxidizer-rich region are not available but would be useful for improving

the analysis and the understanding.

The HDPE-N_2O results (see Fig. 25(b)) confirm what already observed for the HDPE-LOX tests. Reactive and frozen throat erosion rates are extremely similar in fuel-rich conditions, with differences always below 10%. Approaching stoichiometric conditions, relevant gas-phase reaction effects start to be visible. Here, the improved agreement with respect to the experimental data including reactions is more evident than for the HDPE-LOX cases, with the numerical data always falling inside the experimental uncertainty for tests C-1 to C-5 (see Table 3).

VII. Conclusions

In this work, graphite nozzle heating and erosion in hybrid rockets burning HDPE and two different oxidizers (i.e., oxygen and nitrous oxide) have been experimentally and numerically investigated. In particular, results obtained from a detailed parametric numerical analysis have been used to derive closed-form regression laws for nozzle throat erosion and wall temperature depending on chamber pressure and mixture ratio. The regression laws proposed are ready for use, representing a useful tool for hybrid rocket preliminary design and analysis assumed that:

- the oxidizer is either nitrous oxide or oxygen
- the HRE combustion chamber design ensures a sufficiently good mixing and complete combustion (i.e., unitary combustion efficiency)
- the HRE burning time is sufficiently long to reach steady-state conditions in terms of nozzle throat heating
- gas-phase reactions effects on nozzle ablation are negligible (i.e., fuel-rich to near-stoichiometric mixture ratio conditions)

The ranges of chamber pressure and equivalence ratio under which the regression laws have been derived are 10 to 50 bar and 0.34 to 3.4, respectively. The work has been complemented by validation against experimental data.

Regarding the throat erosion regression law, pressure effects have been modeled through a classical power law whose exponent has been shown to be affected primarily by mixture ratio and nozzle geometry, and only secondarily by the oxidizer type. In particular, the pressure exponent is lower at oxidizer-rich conditions, independently from nozzle geometry and oxidizer type, then gradually increasing moving towards stoichiometric and fuel-rich conditions. The pressure exponent value at fixed mixture ratio conditions is strongly dependent on the nozzle geometry, while it is only slightly affected by the specific oxidizer. Anyway, the oxidizer type has a relevant impact on the throat erosion rate absolute value. In fact, an approximately 50% lower throat erosion rate than that with oxygen is reported in case of low oxygen-containing oxidizers, such as nitrous oxide, employing the same operative conditions and using the same nozzle geometry. In addition, the nozzle throat erosion rate, as well as the throat wall temperature, is always maximum at oxidizer-rich conditions, differently from the propellant flame temperature which always peaks at slightly fuel-rich conditions. This confirms that the nozzle throat heating and ablation processes are primarily influenced by the exhaust gas composition and only secondarily by the propellant flame temperature.

A practical application of the closed-form regression laws for fast evaluation of the transient thermal heating and thermal penetration thickness in an ablative TPS has been presented and discussed. The approach employs the derived throat erosion rate and wall temperature regression laws, which are used as time-variable Dirichlet boundary conditions in a one-dimensional transient heat solver. Simulations results slightly overestimate the experimental throat wall temperatures in the early transient of the burn due to the lack of complete boundary coupling between the CFD and the one-dimensional transient heat solver, but provide accurate results in terms of in-depth temperatures as a steady-state condition is approached. Anyway, in case extremely small nozzle dimension and/or TPS thickness are considered, the proposed approach starts to lack in terms of predictive capabilities, with the experimental data overestimated by the numerical results. Anyway, the present simplified approach still represents a good solution for a rapid evaluation of the nozzle in-depth heating, giving valuable information about the thermal penetration thickness, which is of fundamental importance for the ablative TPS sizing and design.

Finally, an analysis of gas-phase reactions effects on the throat erosion process has been performed in order to clearly identify the possible limitations of the proposed closed-form regression laws (computed assuming a frozen flow). Such effects are negligible at fuel-rich conditions (less than 10% variation in terms of nozzle throat erosion rate), while they become relevant moving towards oxidizer-rich mixture ratios. In general, the agreement between the numerical results and the experimental data at near-stoichiometric conditions is improved by including gas-phase reaction effects. However, some discrepancies are still obtained at oxidizer-rich conditions, where the few available experimental data, which are affected by non-negligible uncertainties, are overestimated by the present analysis.

Appendix

A. Transient heat conduction solver verification

The one-dimensional transient heat conduction solver has been verified by performing simulations of a semi-infinite planar slab with constant thermal properties. The exact solution of the semi-infinite slab problem with uniform initial temperature $T_{s,0}$, constant recession rate $\dot{r}$, and boundary temperature equal to T_w reads [49]:

$$\frac{T - T_{s,0}}{T_w - T_{s,0}} = \frac{1}{2}\left[\mathrm{erfc}\left(\frac{x + \dot{r}\,t}{2\sqrt{\alpha t}}\right) + \exp\left(-\frac{x\dot{r}}{\alpha}\right)\mathrm{erfc}\left(\frac{x - \dot{r}\,t}{2\sqrt{\alpha t}}\right)\right] \tag{23}$$

where $\alpha = k_s/(\rho_s c_s)$ is the solid thermal diffusivity, T_w=2500 K, and $T_{s,0}$=298.15 K. Figure 26 shows that the agreement between the exact and computed solution is excellent both without and with recession.

Additionally, the transient heat conduction solver has been checked out for a cylindrical case. In particular, the numerical solution has been compared with the analytical solution of the heat equation in a hollow cylinder with an imposed temperature T_w at the inner boundary and an adiabatic outer wall. The initial material temperature is $T_{s,0}$, thermal properties are assumed to be constant with temperature (as in the previous case), and the inner surface is not

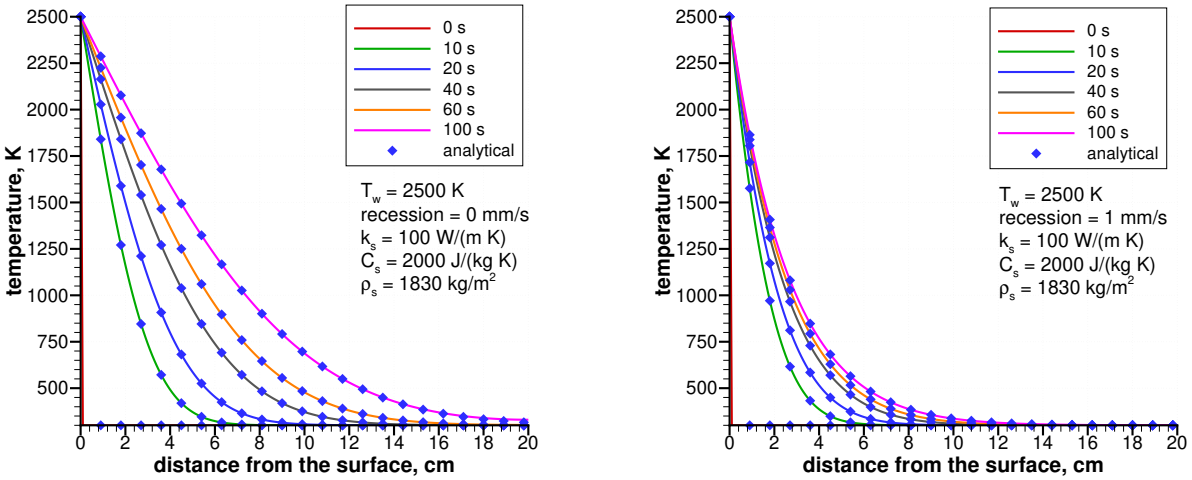

(a) Without surface recession.

(b) Including surface recession.

Figure 26 Verification of the one-dimensional transient heat conduction solver against analytical solutions employing a planar coordinate system.

eroding. The analytical solution writes as [50]:

$$T = T_\mathrm{w} + \frac{\pi^2}{2} T_\mathrm{w} \sum_{m=1}^{\infty} \exp\left(\frac{-\beta_m^2 \alpha t}{R_1^2}\right) \frac{\beta_m J_0^2(\beta_m) \left(J_0\left(\beta_m \frac{r}{R_1}\right) Y_1\left(\beta_m \frac{R_2}{R_1}\right) - J_1\left(\beta_m \frac{R_2}{R_1}\right) Y_0\left(\beta_m \frac{r}{R_1}\right) \right) \left(J_1(\beta_m) Y_1\left(\beta_m \frac{R_2}{R_1}\right) - J_1\left(\beta_m \frac{R_2}{R_1}\right) Y_1(\beta_m) \right)}{J_0^2(\beta_m) - J_1^2\left(\beta_m \frac{R_2}{R_1}\right)} \tag{24}$$

where J_i and Y_i are Bessel functions of the first and second kind, respectively, β_m are the eigenvalues of the problem, r is the radial coordinate calculated from the center of the cylinder, and R_1 and R_2 are the inner and outer cylinder radius, respectively [50]. Figure 27 shows the good agreement between the exact and computed solution also in case of cylindrical coordinates.

References

[1] Altman, D., and Holzman, A., "Overview and History of Hybrid Rocket Propulsion," *Fundamentals of Hybrid Rocket Combustion and Propulsion*, Vol. 218, edited by K. Kuo and M. Chiaverini, AIAA, Reston, VA, 2007, pp. 1–36. https://doi.org/10.2514/5.9781600866876.0001.0036.

[2] Kuo, K., and Houim, R., "Theoretical Modeling and Numerical Simulation Challenges of Combustion Processes of Hybrid Rockets," *AIAA*, paper 2011-5608, 2011. https://doi.org/10.2514/6.2011-5608.

[3] Sutton, G. P., and Biblarz, O., "Hybrid Propellant Rocket Propulsion," *Rocket Propulsion Elements*, John Wiley and Sons, Inc., New York, NY, 2001, pp. 592–620.

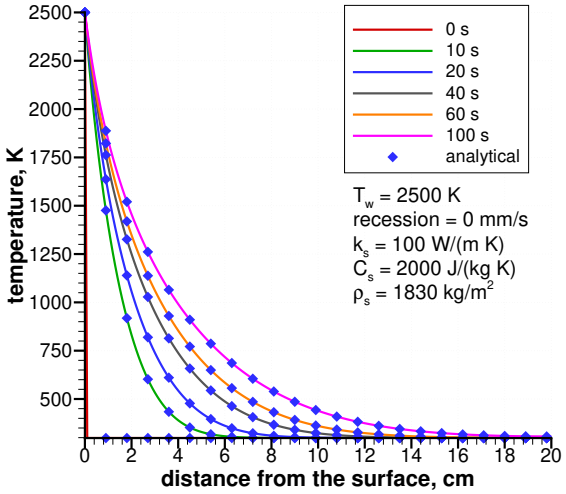

Figure 27 Verification of the one-dimensional transient heat conduction solver against the analytical solution employing a cylindrical coordinate system.

[4] Bunker, R., and Prince, A., "Hybrid rocket motor nozzle material predictions and results," *AIAA*, paper 1992-3591, 1992. https://doi.org/10.2514/6.1992-3591.

[5] Bianchi, D., and Nasuti, F., "Numerical Analysis of Nozzle Material Thermochemical Erosion in Hybrid Rocket Engines," *Journal of Propulsion and Power*, Vol. 29, No. 3, 2013, pp. 547–558. https://doi.org/10.2514/1.B34813.

[6] Bianchi, D., Kamps, L. T., Nasuti, F., and Nagata, H., "Numerical and Experimental Investigation of Nozzle Thermochemical Erosion in Hybrid Rockets," *AIAA*, paper 2017-4640 ,2017. https://doi.org/10.2514/6.2017-4640.

[7] Bianchi, D., Migliorino, M. T., Rotondi, M., Kamps, L., and Nagata, H., "Numerical Analysis of Nozzle Erosion in Hybrid Rockets and Comparison with Experiments," *Journal of Propulsion and Power*, Vol. 38, No. 3, 2022, pp. 389–409. https://doi.org/10.2514/1.B38547.

[8] Davydenko, N., Gollender, R., Gubertov, A., Mironov, V., and Volkov, N., "Hybrid Rocket Engines: The Benefits and Prospects," *Aerospace Science and Technology*, Vol. 11, No. 1, 2007, pp. 55–60. https://doi.org/10.1016/j.ast.2006.08.008.

[9] Story, G. T., Karp, A. C., Nakazono, B., Zilliac, G., Evans, B. J., and Whittinghill, G., "Mars Ascent Vehicle Hybrid Propulsion Effort," *AIAA*, paper 2020-3727, 2020. https://doi.org/10.2514/6.2020-3727.

[10] Ito, S., Kamps, L. T., Yoshimal, S., and Nagata, H., "Evaluation of the Thermal Onset of Graphite Nozzle Erosion," *AIAA*, paper 2020-3755, 2020. https://doi.org/10.2514/6.2020-3755.

[11] Whitmore, S. A., Babb, R. S., Gardner, T. J., LLoyd, K. P., and Stephens, J. C., "Pyrolytic Graphite and Boron Nitride as Low-Erosion Nozzle Materials for Long-Duration Hybrid Rocket Testing," *AIAA*, paper 2020-3740, 2020. https://doi.org/10.2514/6.2020-3740.

[12] Kahraman, B., Karakas, H., Eren, B. N., and Karabeyoglu, A., "Erosion Rate Investigation of Various Nozzle Materials in Hybrid Rocket Motors," *AIAA*, paper 2020-3739, 2020. https://doi.org/10.2514/6.2020-3739.

[13] Kojima, H., Kamps, L. T., Nobuhara, Y., Nagata, H., Valembois, T., and Cottenot, C., "Progress Towards Graphite Nozzle Cooling for Throat Erosion Suppression," *AIAA*, paper 2022-3859, 2022. https://doi.org/10.2514/6.2022-3859.

[14] Bianchi, D., Migliorino, M. T., Nasuti, F., and Onofri, M., "CFD Analysis of Paraffin-Based Hybrid Rockets with Coupled Nozzle Erosion Characterization," *AIAA*, paper 2019-4263, 2019. https://doi.org/10.2514/6.2019-4263.

[15] Zhang, X., Wang, Z., Wang, R., Lu, C., Yu, R., and Tian, H., "Numerical simulation of chemical ablation and mechanical erosion in hybrid rocket nozzle," *Acta Astronautica*, Vol. 192, 2022, pp. 82–96. https://doi.org/https://doi.org/10.1016/j.actaastro.2021.12.012.

[16] Migliorino, M. T., Bianchi, D., and Nasuti, F., "Graphite Nozzle Erosion Trends in Paraffin/Oxygen Hybrid Rockets," *Journal of Propulsion and Power*, Vol. 38, No. 4, 2022, pp. 508–522. https://doi.org/10.2514/1.B38574.

[17] Gallo, G., Kamps, L., Hirai, S., Carmicino, C., and Nagata, H., "One-dimensional Modelling of the Nozzle Cooling with Cryogenic Oxygen Flowing Through Helical Channels in a Hybrid Rocket," *Acta Astronautica*, Vol. 210, 2023, pp. 176–196. https://doi.org/https://doi.org/10.1016/j.actaastro.2023.05.013.

[18] Kamps, L., Hirai, S., Sakurai, K., Viscor, T., Saito, Y., Guan, R., Isochi, H., Adachi, N., Itoh, M., and Nagata, H., "Investigation of Graphite Nozzle Erosion in Hybrid Rockets Using Oxygen/High-Density Polyethylene," *Journal of Propulsion and Power*, Vol. 36, No. 3, 2020, pp. 423–434. https://doi.org/10.2514/1.B37568.

[19] Zavoli, A., Maria Zolla, P., Federici, L., Migliorino, M. T., and Bianchi, D., "Surrogate Neural Network for Rapid Flight Performance Evaluation of Hybrid Rocket Engines," *Journal of Spacecraft and Rockets*, Vol. 59, No. 6, 2022, pp. 2003–2016. https://doi.org/10.2514/1.A35369.

[20] Bianchi, D., Nasuti, F., Onofri, M., and Martelli, E., "Thermochemical Erosion Analysis for Graphite/Carbon-Carbon Rocket Nozzles," *Journal of Propulsion and Power*, Vol. 27, No. 1, 2011, pp. 197–205. https://doi.org/10.2514/1.47754.

[21] Bianchi, D., Turchi, A., Nasuti, F., and Onofri, M., "Chemical Erosion of Carbon-Phenolic Rocket Nozzles with Finite-Rate Surface Chemistry," *Journal of Propulsion and Power*, Vol. 29, No. 5, 2013, pp. 1220–1230. https://doi.org/10.2514/1.B34791.

[22] Turchi, A., Bianchi, D., Nasuti, F., and Onofri, M., "A Numerical Approach for the Study of the Gas-Surface Interaction in Carbon-Phenolic Solid Rocket Nozzles," *Aerospace Science and Technology*, Vol. 27, No. 1, 2013, pp. 25–31. https://doi.org/10.1016/j.ast.2012.06.003.

[23] Bianchi, D., Nasuti, F., and Onofri, M., "Radius of Curvature Effects on Throat Thermochemical Erosion in Solid Rocket Motors," *Journal of Spacecraft and Rockets*, Vol. 52, No. 2, 2015, pp. 320–330. https://doi.org/10.2514/1.A32944.

[24] Bianchi, D., and Nasuti, F., "Navier–Stokes Simulation of Graphite Nozzle Erosion at Different Pressure Conditions," *AIAA Journal*, Vol. 53, No. 2, 2015, pp. 356–366. https://doi.org/10.2514/1.J053154.

[25] Bianchi, D., and Neri, A., "Numerical Simulation of Chemical Erosion in Vega Solid-Rocket-Motor Nozzles," *Journal of Propulsion and Power*, Vol. 34, No. 2, 2018, pp. 482–498. https://doi.org/10.2514/1.B36388.

[26] Bianchi, D., Migliorino, M. T., Rotondi, M., and Turchi, A., "Numerical Analysis and Wind Tunnel Validation of Low-Temperature Ablators undergoing Shape Change," *International Journal of Heat and Mass Transfer*, Vol. 177, No. 121430, 2021. https://doi.org/10.1016/j.ijheatmasstransfer.2021.121430.

[27] Rotondi, M., Migliorino, M. T., Bianchi, D., Pagani, P., and Turchi, A., "Numerical Assessment of Camphor Ablation Flight Relevance in Hypersonic Wind-Tunnel Testing," *Journal of Spacecraft and Rockets*, Vol. 0, No. 0, 2022, pp. 1–18. https://doi.org/10.2514/1.A35318.

[28] Rotondi, M., Migliorino, M. T., and Bianchi, D., *Numerical Analysis of Carbon-based Nozzle Erosion including Transient Heating and Shape Change*, paper 2022-3949, 2022. https://doi.org/10.2514/6.2022-3949.

[29] Anderson, J. D., *Hypersonic and High-Temperature Gas Dynamics*, AIAA, Reston, VA, 2000.

[30] Gordon, S., and McBride, B. J., "Computer Program for Calculation of Complex Chemical Equilibrium Compositions and Applications," Tech. Rep. RP-1311, NASA, 1994.

[31] Bird, R., Stewart, W., and E.N., L., *Transport Phenomena*, John Wiley and Sons, Inc., New York, 1960. https://doi.org/https://doi.org/10.1002/aic.690070245.

[32] Spalart, P. R., and Allmaras, S. R., "A One-Equation Turbulence Model for Aerodynamic Flow," *La Recherche Aerospatiale*, Vol. 1, 1994, pp. 5–21.

[33] Moretti, G., "A Technique for Integrating Two-Dimensional Euler Equations," *Computer & Fluids*, Vol. 15, No. 1, 1987, pp. 59–75. Doi: 10.1016/0045-7930(87)90005-3.

[34] Bianchi, D., Nasuti, F., Martelli, E., and Onofri, M., "A Numerical Approach for High-Temperature Flows over Ablating Surfaces," *AIAA*, paper 2007-4537, 2007. https://doi.org/10.2514/6.2007-4537.

[35] Bradley, D., Dixon-Lewis, G., din Habik, S. E., and Mushi, E., "The oxidation of graphite powder in flame reaction zones," *Symposium (International) on Combustion*, Vol. 20, No. 1, 1985, pp. 931 – 940. https://doi.org/https://doi.org/10.1016/S0082-0784(85)80582-8.

[36] Chelliah, H., Makino, A., Kato, I., Araki, N., and Law, C., "Modeling of Graphite Oxidation in a Stagnation-Point Flow Field Using Detailed Homogeneous and Semiglobal Heterogeneous Mechanisms with Comparisons to Experiments," *Combustion and Flame*, Vol. 104, No. 4, 1996, pp. 469–480. https://doi.org/10.1016/0010-2180(95)00151-4.

[37] Nagle, J., and Strickland-Constable, R. F., "Oxidation of Carbon Between 1000–2000°C," *Proceedings of the Fifth Carbon Conference*, Vol. 1, Pergamon, New York, 1998, pp. 154–164.

[38] Keswani, S. T., and Kuo, K. K., "Validation of an Aerothermochemical Model for Graphite Nozzle Recession and Heat-Transfer Processes," *Combustion Science and Technology*, Vol. 47, No. 3-4, 1986, p. 177–192. https://doi.org/10.1080/00102208608923872.

[39] Bianchi, D., and Nasuti, F., "Carbon-Carbon Nozzle Erosion and Shape-Change Effects in Full-Scale Solid-Rocket Motors," *Journal of Propulsion and Power*, Vol. 28, No. 4, 2012, pp. 820–830. https://doi.org/10.2514/1.B34267.

[40] Kamps, L. T., Sakurai, K., Ozawa, K., and Nagata, H., "Investigation of Graphite Nozzle Erosion in Hybrid Rockets Using N2O/HDPE," *AIAA*, paper 2019-4264, 2019. https://doi.org/10.2514/6.2019-4264.

[41] Kamps, L., Saito, Y., Kawabata, R., Wakita, M., Totani, T., Takahashi, Y., and Nagata, H., "Method for Determining Nozzle-Throat-Erosion History in Hybrid Rockets," *Journal of Propulsion and Power*, Vol. 33, No. 6, 2017, pp. 1369–1377. https://doi.org/10.2514/1.B36390.

[42] Saito, Y., Kamps, L. T., Komizu, K., Bianchi, D., Nasuti, F., and Nagata, H., "The Accuracy of Reconstruction Techniques for Determining Hybrid Rocket Fuel Regression Rate," *AIAA*, paper 2018-4923, 2018. https://doi.org/10.2514/6.2018-4923.

[43] Kamps, L. T., Hirai, S., Sakurai, K., Viscor, T., Saito, Y., Guan, R., Isochi, H., Adachi, N., Itoh, M., and Nagata, H., "Investigation of Graphite Nozzle Erosion in Hybrid Rockets Using O2/C2H4," *AIAA*, paper 2018-4531, 2018. https://doi.org/10.2514/6.2018-4531.

[44] Roache, P. J., "Verification of Codes and Calculations," *AIAA Journal*, Vol. 36, No. 5, 1998, pp. 696–702. https://doi.org/10.2514/2.457.

[45] Bonfiglioli, A., and Paciorri, R., "Convergence Analysis of Shock-Capturing and Shock-Fitting Solutions on Unstructured Grids," *AIAA Journal*, Vol. 52, No. 7, 2014, pp. 1404–1416. https://doi.org/10.2514/1.J052567.

[46] Bartz, D., "A Simple Equation for Rapid Estimation of Rocket Nozzle Convective Heat Transfer Coefficient," *Journal of Jet Propulsion*, Vol. 27, No. 1, 1957, pp. 49–53. https://doi.org/10.2514/8.12572.

[47] Yetter, R. A., Dryer, F. L., and Rabitz, H., "A Comprehensive Reaction Mechanism For Carbon Monoxide/Hydrogen/Oxygen Kinetics," *Combustion Science and Technology*, Vol. 79, No. 1-3, 1991, pp. 97–128. https://doi.org/10.1080/00102209108951759.

[48] Kim, T. J., Yetter, R. A., and Dryer, F. L., "New Results on Moist CO Oxidation: High Pressure, High Temperature Experiments and Comprehensive Kinetic Modeling," *Symposium (International) on Combustion*, Vol. 25, No. 1, 1994, pp. 759–766. https://doi.org/https://doi.org/10.1016/S0082-0784(06)80708-3.

[49] Baer, D., and Ambrosio, A., "Heat Conduction in a Semi-Infinite Slab with Sublimation at the Surface," *Planetary and Space Science*, Vol. 4, 1961, pp. 436 – 446. https://doi.org/https://doi.org/10.1016/0032-0633(61)90150-7.

[50] Nallapaneni, S., and Beck, J., "ExACT – Exact Analytical Conduction Toolbox," Tech. Rep. R12B10T0, University of Nebraska–Lincoln, 2014.